DEPARTMENT OF PHYSICS
UNIVERSITY OF JYVÄSKYLÄ
RESEARCH REPORT No. 5/2015

Spectroscopy of ^{199,201}At

by

Kalle Auranen

Academic Dissertation
for the Degree of
Doctor of Philosophy

To be presented, by permission of the
Faculty of Mathematics and Science
of the University of Jyväskylä,
for public examination in Auditorium YAA303 of the
University of Jyväskylä on June 5, 2015
at 12 o'clock noon

Jyväskylä, Finland
May 2015

Abstract

Auranen, Kalle
Spectroscopy of ^{199,201}At
Jyväskylä: University of Jyväskylä, 2015, 80 p.
Department of Physics Research Report No. 5/2015
ISSN: 0075-465X; 5/2015
ISBN: 978-951-39-6172-5 (paper version)
ISBN: 978-951-39-6173-2 (electronic version)
Diss.

The excited states of ^{199}At and ^{201}At were studied using fusion evaporation reactions, a gas-filled recoil separator and various tagging methods. The level scheme of ^{201}At was extended a lot including a cascade of magnetic dipole transitions, that is suggested to form a shears band. In addition, a $^{29}/_{2}^{+}$ [$T_{1/2} = 3.39(9)$ µs] isomeric state was observed. The $^{29}/_{2}^{+}$ state is suggested to originate from the $\pi(h_{9/2}) \otimes |^{200}\mathrm{Po}; 11^{-}\rangle$ configuration, and it depopulates through 269-keV $E2$ and 339-keV $E3$ transitions. In both nuclei ^{199,201}At we have observed also the isomeric $^{1}/_{2}^{+}$ [$T_{1/2} = 273(9), 45(3)$ ms, respectively] intruder state, that is suggested to originate from the $\pi(s_{1/2})^{-1}$ configuration. The $^{1}/_{2}^{+}$ state decays through 103- keV and 269-keV $E3$ transitions in ^{199,201}At, respectively. In both nuclei the $^{1}/_{2}^{+}$ state is fed from $^{3}/_{2}^{+}$ and $^{5}/_{2}^{+}$ states, which are suggested to originate from the $\pi(d_{3/2})^{-1}$ and $\pi(d_{5/2})^{-1}$ configurations, respectively.

Keywords: nuclear structure, nuclear spectroscopy, γ-ray spectroscopy, shears band, neutron-deficient nuclei, recoil-decay tagging

Author's address Kalle Auranen
Department of Physics
University of Jyväskylä
Finland

Supervisors Dr. Juha Uusitalo
Department of Physics
University of Jyväskylä
Finland

Dr. Sakari Juutinen
Department of Physics
University of Jyväskylä
Finland

Reviewers Prof. Robert Page
Department of Physics
University of Liverpool
United Kingdom

Dr. Araceli Lopez-Martens
CSNSM, IN2P3-CNRS
Orsay Campus
France

Opponent Prof. Paul Campbell
Nuclear Physics Group
University of Manchester
United Kingdom

Preface

This work is based on two publications [Auranen14] and [Auranen15], and it has been carried out at the Accelerator laboratory of the University of Jyväskylä between the years 2011-2015. Financial support from the doctoral programme in PArticle- and NUclear physics (PANU) is gratefully acknowledged.

I have had a privilege to carry out the work presented here as a member of the Nuclear Spectroscopy group. I would like to thank all of the group members for the professional yet relaxed working atmosphere. Especially I would like to express my gratitude to my supervisors Dr. Juha Uusitalo and Dr. Sakari Juutinen for all of the professional guidance and educational conversations we have had during these years. In addition, a great thank you goes to whole astatine/bismuth team. Also I would like to thank Dr. Ulrika Jakobsson and Dr. Pauli Peura for helping me with various practical things such as data analysis and the maintenance of our experimental devices. Moreover, I might have learned some physics from you.

Finally, I want to thank my family, friends and of course my dear significant other Sanna for all of the great joy and support you have brought to my life.

Kalle Auranen
Jyväskylä, June, 2015

Contents

Chapter 1

Introduction

"In this field, almost everything is already discovered, and all that remains is to fill a few holes." With these words Johann Philipp Gustav von Jolly advised Max Planck to not to go into physics in 1874 [nat08]. A few decades later in 1896, Henri Becquerel was making an experiment in the field of fluorescence. He placed some uranium salt near a photographic plate, and the plate darkened despite some material in between. Soon Becquerel realized that this had nothing to do with fluorescence. He had accidentally discovered a completely new phenomenon, radioactivity. In further studies several scientists, Marie and Pierre Curie to name two, discovered new radioactive materials, and also several new types of radioactivity [Centnerszwer15]. A breakthrough in the understanding of the structure of the atom came a little later in 1909, when Ernest Rutherford along with Hans Geiger and Ernest Marsden carried out the famous gold-foil experiment. In this study they observed that some α particles scattered back from a thin gold foil. From this they concluded that an atom must have a small, heavy, positively charged nucleus [Rutherford11]. Ever since the atomic nucleus has been under research.

An atomic nucleus consists of Z protons and N neutrons. To date 118 elements, and over 3800 different isotopes of them are known [Magill12]. Out of these isotopes around 250 are stable, but in nature roughly 80 nuclei can be found

that are not stable, but instead are long living. The rest of the known nuclei are artificial, and they are produced in laboratories. Producing artificial isotopes may require complex devices and long experiments, typically days or weeks. The purpose of these experiments is to produce fundamental information about the structure of matter. The region around lead nuclei and the $Z = 82$ magic shell gap offers a large variety of interesting nuclear phenomena. These include, for example, shape coexistence and a sudden change in ground-state deformation between neighboring nuclei. Also sudden changes in the ground-state spin and parity between two neighboring nuclei occur in this region. Spherical or nearly spherical shapes can be found in even-mass polonium nuclei close to the $N = 126$ shell closure. When moving from the shell closure towards the neutron drip line and the $N = 104$ neutron midshell, a change from spherical to oblate-deformed and onwards to prolate-deformed collective structures occurs. Similar behavior can be anticipated for astatine nuclei, hence those can be described as an odd proton around a polonium core [Heyde83, Wood92, Julin01, Helariutta99, Van de Vel03].

In this work two nuclei, ^{199}At and ^{201}At, were studied using fusion-evaporation reactions and a gas-filled recoil separator. Experimental studies of astatine nuclei are needed in order to test different theoretical models and to gain information about the structure of nuclear matter. In this work we were able to extend the knowledge in ^{199,201}At that is related to an isomeric $1/2^+$ intruder state, and an isomeric $29/2^+$ state. In addition, a band originating from a shears mechanism was observed in ^{201}At.

When a proton is excited from the $s_{1/2}$ state across the magic $Z = 82$ proton shell gap, an intruder $1/2^+$ isomeric state can be created. Such isomeric states are well known through out the bismuth isotopes ([Andreyev04], and references therein). These states in neutron deficient bismuth isotopes show a typical behavior for intruder states in this region. The excitation energy of the state decreases as a function of decreasing neutron number. In astatine nuclei the respective state was first observed in the isotope ^{197}At [Coenen86]. The $1/2^+$ state becomes the ground state in ^{195}At [Kettunen03b, Nyman13], and it is also observed as a ground state in the isotopes ^{191,193}At [Kettunen03a]. The $1/2^+$ state was also observed recently in ^{199}At [Jakobsson13]. However this information is scarce, and there is some room for improvements. In francium nuclei the corresponding state has been observed in the isotopes ^{199,201,203,205}Fr

[Uusitalo05, Jakobsson13, Jakobsson12, Kalaninová13, Uusitalo13]. In ^{199}Fr it is likely that the $1/2^+$ state becomes the ground state.

To date, there are several observations of isomeric $^{29}/_{2}^+$ states in neutron deficient odd mass astatine nuclei. These observations include the astatine isotopes ^{199,205,209,211}At [Jakobsson10, Davie84, Sjoreen76, Bergström70]. These observations are uniform, but a lack of knowledge exists what comes to the isotopes ^{197,201,203,207}At. In the astatine isotopes ^{197,199}At on top of the isomeric $^{13}/_{2}^+$ state there is a strongly coupled rotational band [Jakobsson10]. In ^{203}At this structure disappears [Dybdal83], but the existing information for the intermediate nucleus ^{201}At is scarce [Dybdal83], so the existence of the rotational structure remains as an open question. As mentioned in the preceding section, the $1/2^+$ state becomes the ground state in ^{195}At and lighter isotopes, hence in these nuclei the scheme of observed excited states changes.

At the early 1990s rotational-like bands of $M1$ transitions were found in nearly spherical nuclei. One of the first cascades was found in ^{199}Pb. The conformity of the γ-spectra of these bands were remarkable, almost like in the superdeformed bands. To this day, over 50 such cases have been found mainly in $^{191,\ldots,202}$Pb and $^{198,\ldots,203}$Bi [Clark00]. Some examples in other mass regions are known, such as cadmium [Clark99], tin [Jenkins98, Gadea97] and samarium [Brandolini96] nuclei. However, only a few such bands have been found in nuclei heavier than bismuth, these are ^{205}Rn [Novak99], ^{204}At and ^{206}Fr [Hartley08]. These so-called shears bands can be explained by Frauendorf's tilted-axis cranking model [Frauendorf93].

Chapter 2

Physics background

The atomic nucleus consists of protons and neutrons, collectively called nucleons. The nucleons are bound together by the strong force. The strong force is one of the four fundamental interactions known in the nature. The strong force is understood to have a complex nature, hence a complete nuclear theory does not exist yet. However, significant progress has been and is being made in the field of nuclear models. One of the earliest nuclear models was the *liquid-drop model*, that was introduced in the 1930s. In this very simple model the nucleus is considered as a collection of protons and neutrons forming a droplet of incompressible fluid. The liquid-drop model describes well the general trends of the nuclear binding energy. However, it appears to fail near certain proton and neutron numbers, namely magic numbers. Efforts to understand this observation led to the development of the nuclear *shell model*.

This chapter presents the basics of the nuclear structure. The nuclear shell model will be presented with little more detail, but also the *Nilsson model* will be introduced. Also one specific mechanism, namely the *shears mechanism*, relevant for the results of this work will be introduced. Sections 2.2, 2.3 and 2.6 are written on the basis of [Lilley02], but the same information can be found in any of the introductory nuclear physics textbooks.

2.1 Experimental evidence for the shell structure

There are a large number of anomalies in several observables around the nuclear chart. These anomalies are concentrated to nuclei where either the proton or the neutron number (or both) is 2, 8, 20, 28, 50, 82 or 126. Perhaps the most simple example is the number of stable isotopes for each element. For example when the proton number is 50, the number of stable isotopes is larger than the average number of stable isotopes for other elements in this region. A few other examples of these anomalies are presented in Fig. 2.1. In panel (a) the lowest 2^+ state level energies are presented for even $N = Z$ nuclei. From the figure one may observe that these level energies are anomalously high for nuclei with $N = Z = 2, 8, 20$ or 28. In panel (b) one neutron separation energies S_n are presented for krypton nuclei. In this figure one may see a larger drop in the nuclei around $N = 50$ than in the neighboring ones. A similar drop can be seen around $Z = 82$ nuclei in panel (c), where one-proton separation energies S_p are presented for $N = 122$ nuclei. Panel (d) presents the α-decay Q-values (energy released in the α-decay) for odd mass astatine isotopes. Also in this observable there is a large anomaly around $N = 126$. Based on these observations it is evident that in nuclei having neutron (or proton) number 2, 8, 20, 28, 50, 82 or 126, several observables show behavior that can only be understood through the nuclear shell model.

2.2 Shell model

The idea of the shell model is that the protons and the neutrons are in ordered quantum states in a potential well that is the same for all of the nucleons. In reality, many nuclei behave as if most of the nucleons form a core, and low-energy excited states are formed by some nucleons outside the core. This scheme is analogous to the atom, where electrons are arranged into shells, and the chemical properties are determined by a few valence electrons. According to classical expectations, this model should not perform well, since the nucleon is not very small compared to the size of the nucleus. One might expect nucleon-nucleon collisions to occur, hence the picture where nucleons move in well-defined quantum states in an average potential well would not

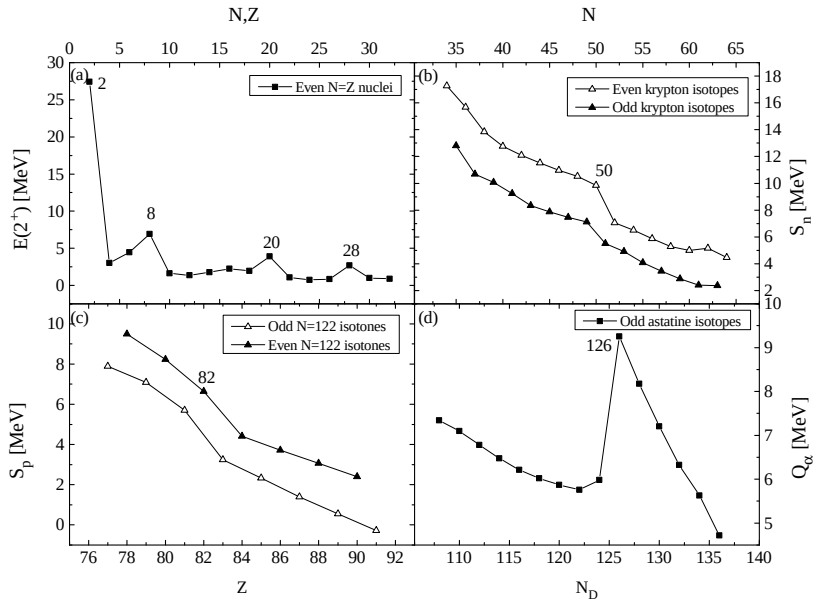

Figure 2.1: Some examples of the shell effects: (a) The energies of the lowest 2^+ states in even N=Z nuclei. (b) One neutron separation energies in the krypton nuclei. (c) One proton separation energies in the N=122 nuclei. (d) α-decay Q-values in the odd mass astatine isotopes. The presented data are extracted from the NuDat2.6 database [Nudat2.6].

be useful. However, the nucleus is a pure quantum-mechanical object and therefore the nucleon-nucleon collisions inside the nucleus are strictly limited due to the Pauli's exclusion principle.

The potential energy U experienced by a nucleon in a nucleus is formed by its interactions with other nucleons. Therefore the radial shape of the potential will be similar to the nuclear density. In other words, it is rather constant inside the nucleus far from the surface. On the surface the potential disappears over a distance of roughly the range of strong interaction. The potential energy is often parametrized in the following way:

$$U(r) = \frac{-U_0}{1 + e^{(r-R)/a}}. \tag{2.1}$$

This is known as the Woods-Saxon potential. Here R is the radius where the

potential has dropped to half of its value at the center of the nucleus. The diffuseness of the nuclear surface is marked with a. The three dimensional Schrödinger equation can be solved using the parametrization 2.1 for the potential energy, and the obtained energy states are presented in Fig. 2.2(b).

The labels of single particle states in Figs. 2.2(a) and (b) follow the notation Nl. Here $N = 1, 2, 3 \ldots$ is the main quantum number giving the number of nodes in the wave function of each state. The angular momentum quantum number $l = 0, 1, 2 \ldots$ is denoted with labels $s, p, d, f, g, h, i, j \ldots$. For each l-state there are $2l + 1$ substates corresponding to different allowed orientations of the angular momentum vector along a given direction. According to the exclusion principle the A nucleons are filled in ascending order to l-states, each capable of taking $2(2l + 1)$ protons or neutrons. A magic number occurs when there is a gap between two consecutive states.

Fig. 2.2 shows the obtained magic numbers using two different potentials, a simple three dimensional square well (a) and the Woods-Saxon potential (b). Both of these models appear to reproduce the three lowest magic numbers, but neither of the wells is capable of explaining the magic numbers higher than the third one. In the 1940s many efforts were made, and several well shapes were tried, but none of these was capable of explaining the deviation between the experimental magic numbers and the calculated ones. Not until 1949 when by Mayer and by Haxel, Jensen and Suess the correct magic numbers were obtained. This was done by introducing a spin-orbit coupling term into the Woods-Saxon potential.

The spin-orbit potential has the form $-U_{SO}(r)\vec{l} \cdot \vec{s}$, where $\vec{s}$ is the spin angular momentum. Fig. 2.2(c) shows the single-particle states obtained by solving the Shrödinger equation when the spin orbit coupling term is added to the Woods-Saxon potential. Labeling of the states follows the notation Nl_j, where N and l are as presented above, and $\vec{j} = \vec{l} + \vec{s}$ is the total angular momentum. Protons and neutrons have a spin of $s = 1/2$, therefore each state can have a total angular momentum of $j = l \pm 1/2$. Each j state has now $2j + 1$ substates, thus each j-state can contain up to $2j + 1$ nucleons of each kind. The spin-orbit splitting can be easily deduced, because

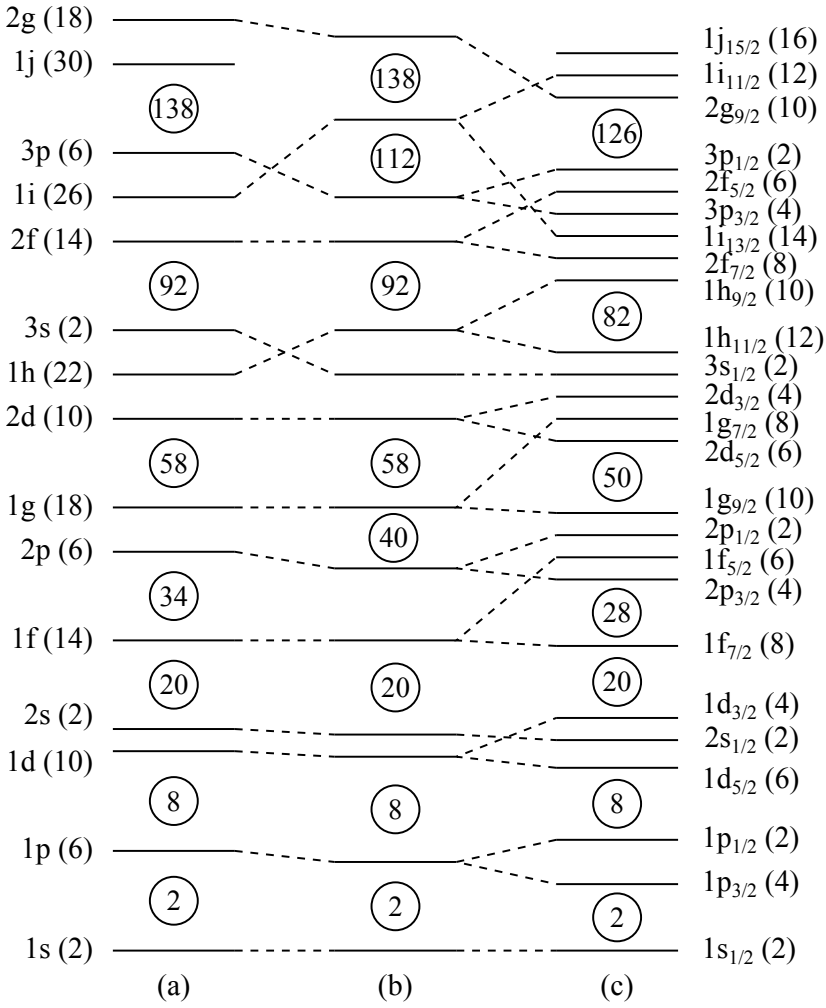

Figure 2.2: Schematics of the single particle states calculated for different forms of the nuclear potential: (a) Infinite square well, (b) Woods-Saxon potential and (c) Woods-Saxon potential plus spin-orbit coupling. Circled numbers represent the magic numbers corresponding to closed shells. Numbers in parentheses indicate the maximum allowed number of protons or neutrons for each state.

$$\vec{j}^2 = (\vec{l} + \vec{s})^2 = \vec{l}^2 + \vec{s}^2 + 2\vec{l}\cdot\vec{s}. \tag{2.2}$$

From this it immediately follows for the expectation value $\langle \vec{l}\cdot\vec{s} \rangle$, that

$$\langle \vec{l}\cdot\vec{s} \rangle = \frac{1}{2}\left[j(j+1) - l(l+1) - s(s+1) \right] \hbar^2. \tag{2.3}$$

Keeping in mind that $s = 1/2$, hence $j = l \pm 1/2$, after direct substitution it follows that

$$\langle \vec{l}\cdot\vec{s} \rangle = \begin{cases} \frac{1}{2} l \hbar^2 & \text{when } j = l + 1/2 \\ -\frac{1}{2}(l+1)\hbar^2 & \text{when } j = l - 1/2 \ (l \neq 0) \end{cases}. \tag{2.4}$$

Therefore the spin-orbit splitting is proportional to $2l + 1$. Comparing columns (b) and (c) in Fig. 2.2, one can easily see the effect of the spin orbit splitting for all of the $l \neq 0$ states.

The shell model describes well the groundstate properties and the properties of a few lowest excited states for various nuclei close to magic numbers. For example in the case of ^{201}At (Z=85, N=116) the protons fill the single-particle states up to the magic shell gap $Z = 82$, and the remaining three protons occupy the $1h_{9/2}$ orbital. Nucleons have a strong tendency to form pairs, and therefore the neutrons and protons couple to 0^+ when possible, and the ground-state spin I and parity π are determined by the odd proton in the $1h_{9/2}$ orbital. Parity is a property of the wave function $\Psi(\vec{r})$ describing each single-particle state. While the potential U is invariant (i.e. $U(\vec{r}) = U(-\vec{r})$), the wave function describing the system has the property of $\Psi(\vec{r}) = \pm\Psi(-\vec{r})$. This means that there are two different types of wave functions, those with even parity (+) and those with odd parity (-). In practice the parity is given by the equation $\pi = (-1)^l$. In the case of the above example, $l = 5$ corresponds to negative parity, while the spin of the ground state is $9/2$. The first excited state corresponds to the case when the 3rd proton is excited from the $1h_{9/2}$ state to the $2f_{7/2}$ state corresponding to spin and parity of $I^\pi = 7/2^-$. These two spin and parity assignments match the experimental findings, as we will

see later in section 4.2. The nuclear shell model performs well when predicting the properties of the ground state and the lowest excited state, especially in the vicinity of closed shells. However, there are modes of excitation that are better described as *collective vibrations* or *rotations* of the nucleus.

2.3 Collective states

2.3.1 Vibrational States

The liquid drop model assumes the nucleus to be spherical in its ground state. Any change in the deformation would increase the potential surface term from the spherical minimum. For small deformations, the increase in the potential energy is parabolic, like for a harmonic oscillator. Therefore it is possible for the nucleus to oscillate around the spherical minimum. It is possible to solve the Shrödinger equation for these states using an appropriate harmonic oscillator potential. These states can be described as vibrations of a liquid drop. Any surface in three dimensions can be expressed by the radius as a sum of spherical harmonics [Preston62]

$$R = R_0 \left[1 + \sum_{\lambda=0}^{\infty} \sum_{m=-\lambda}^{\lambda} \alpha_{\lambda m}(t) Y_\lambda^m(\theta, \phi) \right], \tag{2.5}$$

where θ and ϕ are the angular co-ordinates of a point on the surface, and the parameters α are the time dependent amplitudes describing the vibration around the average radius R_0. The expansion is written in terms of *multipoles* λ, a few lowest multipoles are presented in Fig. 2.3. Each type of vibration has its own characteristic frequency ω_λ. The energy of the vibration is quantized in the units of $\hbar\omega_\lambda$, and a single energy quantum is often called a phonon. The spin and parity of the phonon are λ and $(-1)^\lambda$, respectively. The three lowest modes of the vibration are:

λ=0 (monopole): This mode is forbidden in the simple liquid drop model, because in the model the nuclear droplet is assumed to be incompressible. However, this is not the case in reality. Nuclear matter is compressible,

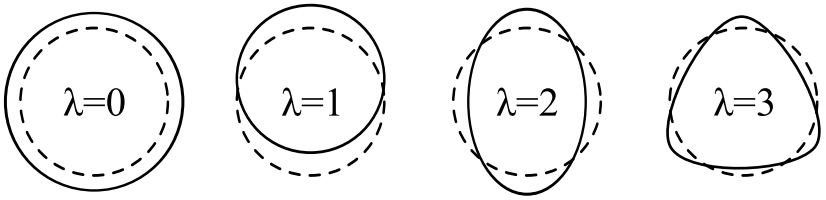

Figure 2.3: A few lowest vibrational modes of a spherical system. Multipoles $\lambda = 0, 1, 2, 3$ correspond to monopole, dipole, quadrupole and octupole vibrations, respectively. The dashed line represents the equilibrium state.

but the restoring force is very strong. Therefore these 0^+ states will be high in energy, typically at several hundred MeV.

λ=1 (dipole): The dipole mode gives a shift to the center of mass. However, there are no external forces. This mode is only allowed if protons and neutrons move in opposite directions in the nucleus. In this type of vibration the total center of mass stays fixed, but the proton center of mass and neutron center of mass oscillate around the equilibrium point. However, the separation of protons and neutrons is restricted by the strong force, and therefore collective 1^- dipole states can be found around $10 - 20$ MeV excitation energy.

λ=2 (quadrupole): This mode requires neither the compression of nuclear matter, nor the separation of different nucleons. Therefore these vibrational states can be found at lower excitation energy. Quadrupole vibrations involve two different types. The one where the whole nucleus vibrates is called the giant quadrupole resonance. These states are typically found at excitation energies of greater than 10 MeV. The other quadrupole vibration type is such that only the nucleons near the surface vibrate. Surface quadrupole vibrations occur at much lower excitation energy than the giant quadrupole resonance. A simple example of these vibrations is when the 0^+ ground state of an even-even nucleus is excited to the 2^+ state by adding of one quadrupole phonon.

λ=3 (octupole): When an octupole phonon is coupled to the 0^+ ground state of an even-even nucleus, a 3^- excited state is created. The 3^- state at the excitation energy of 2.61 MeV in ^{208}Pb is an example of the collective octupole vibration. Coupling two octupole phonons to the nucleus raises

it to an excitation energy high enough to break a nucleon pair. Therefore the treatment of such situations is complicated.

2.3.2 Rotational States

Quantum mechanically a collective rotation can only be observed in deformed nuclei. A perfectly spherical nucleus has no preferred direction in space, hence rotating it does not create an observable change. Elliptically shaped nuclei can rotate around one of the axes, but not around the symmetry axis. In the ground state of an even-even nucleus the nucleons couple to 0^+, hence the angular momentum caused by the rotation is equal to the total angular momentum I of the nucleus. The angular part of the wave function of the excited state can be described as a spherical harmonic function $Y_I^M(\theta, \phi)$, where M is the $\hat{z}$-projection of the I. The parity of the wave function is therefore $(-1)^I$. Due to mirror symmetry of an ellipsoid with respect to an axis that is perpendicular to the symmetry axis of the nucleus, the allowed values of I contain only odd or even values. For an even-even nucleus the ground state is 0^+, hence the allowed rotational states are $I^\pi = 0^+, 2^+, 4^+ \ldots$. The classical expression for the energy of a body with a total moment of inertia $\mathcal{J}$ rotating with frequency ω is $E = \frac{1}{2}\mathcal{J}\omega^2$. Substituting the quantum mechanical expectation value $I(I+1)\hbar^2$ for the square of rotational angular momentum $\mathcal{J}\omega$, one obtains the expression

$$E(I) = \frac{I(I+1)\hbar^2}{2\mathcal{J}} \tag{2.6}$$

for the excited state level energies of a collectively rotating nucleus. This expression assumes that the nucleus is a rigid body. In other words, the total moment of inertia is independent of the rotational frequency. This is not the case in reality, but the nuclear matter is "soft" in the sense that the moment of inertia has a tendency to increase when the rotational frequency increases. However, the equation 2.6 works well for a few lowest ($I \lesssim 8\hbar$) excited states in a rotational cascade in well-deformed nuclei.

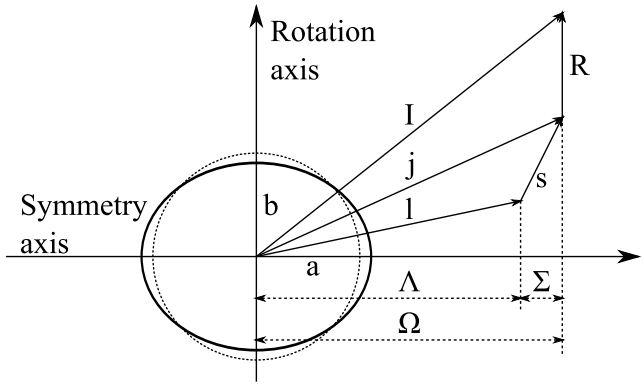

Figure 2.4: An ellipsoid with radius parameters a and b corresponding to prolate deformation of $\beta_2 \approx 0.2$. Also the notation of the states in the Nilsson diagram is presented.

2.4 Nilsson model

On the nuclear chart there are a number of nuclei whose magnitude of quadrupole moment cannot be explained by the spherical shell model. In 1950 James Rainwater suggested [Rainwater50], that these quadrupole moments could be explained, if the nucleus is allowed to have a deformed shape. This led to an extension of the shell model called *Nilsson model* or *deformed shell model*. For a more detailed description of this model, see [Nilsson55] or [Nilsson95].

Figure 2.4 presents an ellipsoid with quadrupole deformation of $\beta_2 \approx 0.2$. The quadrupole deformation is often defined [Bohr98] as

$$\beta_2 = \frac{a-b}{R_{\text{av}}} = \frac{a-b}{\frac{1}{3}(a-2b)}. \tag{2.7}$$

Positive values of β_2 stand for prolate nuclear shapes (cigar-like) and negative β_2 values stand for oblate (disc-like) nuclear shapes. As stated earlier, for each j-state there are $2j+1$ degenerate substates in the case of a spherical potential. However, when the nucleus is deformed this degeneracy will be lost, and each spherical j state will split. In Fig. 2.5 this splitting is presented

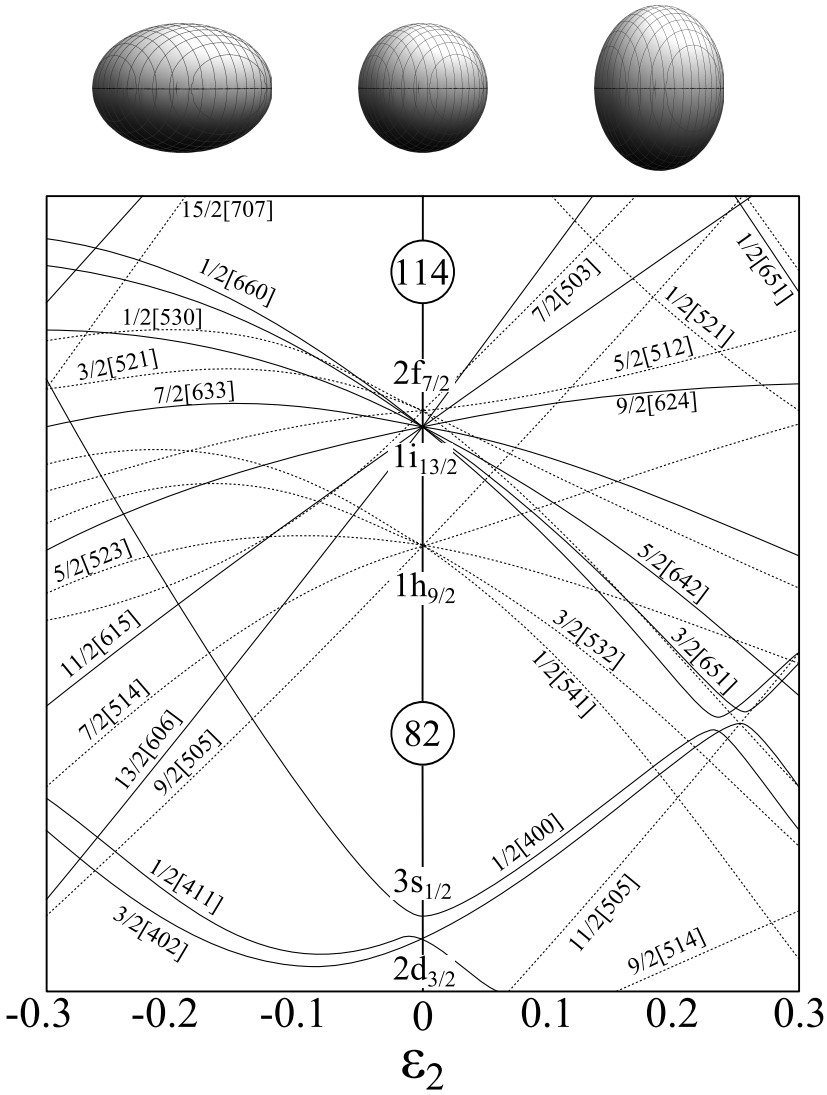

Figure 2.5: A schematic, harmonic-oscillator based, Nilsson diagram for nuclei with proton number close to the magic $Z = 82$ shell closure. Deformation-induced splitting of proton states is presented as a function of quadrupole deformation ε_2. Positive values of ε_2 correspond to prolate deformation and negative values to oblate deformation. $\varepsilon_2 = 0$ corresponds to spherical nuclei, and the respective states are identical to spherical shell model states.

as a function of the quadrupole deformation[1] ε_2 for the harmonic oscillator potential. Because of the splitting, j is no longer a good quantum number, hence a new set of quantum numbers is needed. One generally used set is the asymptotic quantum numbers $\Omega^{\pi}[Nn_r\Lambda]$, where N and π are as described earlier. Ω and Λ are the projections (Fig. 2.4) of j and l with respect to the symmetry axis, respectively. In Fig. 2.4 R stands for the rotation of the nucleus. The last quantum number n_r stands for the number of nodes in the radial part of each state wave function.

In the case of ^{199,201}At the ground state is understood to be nearly spherical, hence it can be described as an odd proton in the $1h_{9/2}$ orbital with $\varepsilon_2 \sim 0$. As we will see later in the section 4.2, in both of these nuclei there is a low-lying $1/2^+$ state, which is understood to originate from the $\pi(s_{1/2})^{-1}$ excitation. This is possible because the $1/2^+[400]$ Nilsson orbital approaches the Fermi surface rapidly as the nucleus gets oblate deformed, see Fig. 2.5.

2.5 Shears mechanism

In the shears phenomenon a (high-j) neutron(s) and proton(s) states are coupled. The coupling results in a total angular momentum vector which does not lie on any of the principal axes. Schematics of this coupling are presented in Fig. 2.6. The angle θ between the proton spin j_π and the neutron spin j_ν is called *the shears angle*. When the excitation energy is increased, the shears angle decreases (like closing shears) increasing the total angular momentum of the system. Hence the name shears band. Once the proton and neutron states are known, the shears angle can be calculated using the semiclassical equation

$$\begin{aligned}\cos\theta &= \frac{\vec{j_\nu}\cdot\vec{j_\pi}}{|\vec{j_\nu}||\vec{j_\pi}|} \\ &= \frac{I(I+1)-j_\nu(j_\nu+1)-j_\pi(j_\pi+1)}{2\sqrt{j_\nu(j_\nu+1)j_\pi(j_\pi+1)}}.\end{aligned} \tag{2.8}$$

[1] $\varepsilon_2 \approx 0.95\beta_2$ [Bohr98].

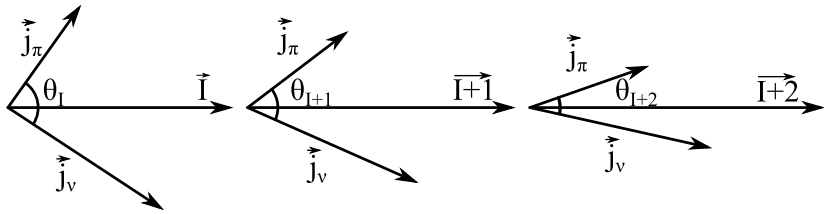

Figure 2.6: Schematics of the angular momentum coupling of the proton and neutron states in a shears band.

States involved in the shears mechanism have typically high angular momentum j, otherwise long cascades typical for shears bands are not possible. A particle-hole coupling is usually needed to achieve these large angular momenta. The deformation of the core must be small enough, otherwise rotational cascades dominate over the shears mechanism. The shears bands have some general properties which may be summarized as follows:

1. The states in the band (far from band crossings) follow the parabolic pattern of $E(I) - E_0 \propto (I - I_0)^2$, where 0 refers to the band-head state.
2. The band is formed from strong[1] $M1$ transitions with weak $E2$ cross overs, typically $^{B(M1)}/_{B(E2)} \gtrsim 20\ \mu_N^2/e^2b^2$, and $B(M1) \sim 2 - 10\ \mu_N^2$.
3. The structures have small quadrupole deformation.
4. Active orbitals must involve high j values.
5. The ratio of the dynamic moment of inertia over $B(E2)$ is large, $>100\ \hbar^2\mathrm{MeV}^{-1}(\mathrm{eb})^{-2}$, when compared to well-deformed ($\sim 10\ \hbar^2\mathrm{MeV}^{-1}(\mathrm{eb})^{-2}$) or superdeformed ($\sim 5\ \hbar^2\mathrm{MeV}^{-1}(\mathrm{eb})^{-2}$) bands.

The text above is a short summary of the annual review publication [Clark00] by R. M. Clark and A. O. Macchiavelli.

[1] Transition strength $B(\sigma L)$ will be defined later in equation 2.14.

2.6 Nuclear decay

Let us consider a radioactive sample of N nuclei. If the probability per time unit for the decay of a given nucleus is λ, the number of decays per time unit is then

$$\frac{\mathrm{d}N}{\mathrm{d}t} = -\lambda N. \tag{2.9}$$

Here the minus sign indicates that the number of nuclei decreases as the time passes, and λ is known as the decay constant. This equation is a first order, separable differential equation and the solution is

$$N(t) = N_0 e^{-\lambda t}, \tag{2.10}$$

where N_0 is the number of nuclei when $t = 0$. Moreover, the decay constant is related to the mean lifetime τ, and to the half-life $T_{1/2}$ of the initial state as follows:

$$T_{1/2} = \frac{\ln 2}{\lambda} = \tau \ln 2. \tag{2.11}$$

If there are decay branches to several final states, a partial half life $T^i_{1/2}$ can be determined for all of the branches i

$$T^{\mathrm{i}}_{1/2} = \frac{T_{1/2}}{b_{\mathrm{i}}}, \tag{2.12}$$

where b_i is the branching ratio. In addition the total decay constant can be expressed as a sum of partial decay constants.

The *exponential decay law* presented above can be applied to all species of nuclear decay. The parent nucleus can change into another nucleus, often called the daughter nucleus, by emitting a particle. This particle can be for example an electron (β^- decay), a positron (β^+ decay), or the nucleus of

a helium atom (α decay). Also proton and neutron emissions are known, as well as fission, where a heavy nucleus splits into two medium heavy nuclei. The exponential decay law also applies to a case where the transitions happen between two different energy states of the same nucleus. This type of transitions can occur in two ways, through either γ-ray emission or internal conversion.

2.6.1 γ-ray emission

An excited state of a nucleus can be depopulated through photon emission, these photons are often called γ rays. The energy of the γ ray E_γ is equal[1] to the energy difference between initial and final states. A γ ray carries away angular momentum L, which is often called *multipolarity*. L can have any integer value greater than zero, photons with angular momentum zero do not exist. γ radiation with angular momentum $L = 1, 2, 3, \ldots$ is often called dipole, quadrupole, octupole,... radiation, respectively. The conservation of angular momentum demands that $\vec{I}_\mathrm{i} = \vec{I}_\mathrm{f} + \vec{L}$, from where follows the selection rule

$$|I_\mathrm{i} - I_\mathrm{f}| \leq L \leq I_\mathrm{i} + I_\mathrm{f}. \tag{2.13}$$

Here I_i and I_f stand for the initial and final state spin, respectively. Electromagnetic transitions can be divided into two types, electric and magnetic. The Parity of the the electric transition is $(-1)^L$ and the parity of the magnetic transition is $(-1)^{L+1}$. In the electromagnetic transition the parity must be conserved, hence one may summarize selection rules for the type of the γ-ray radiation. These selection rules are presented in table 2.1.

According to these rules, typically several transition types are allowed. However, the emission rate is strongly dependent on the multipolarity. In several even-even nuclei for example, transition types $E2$, $M3$, $E4$, $M5$, and $E6$ are allowed for a transition from a 4^+ state to a 2^+ state, but the smallest multipolarity $E2$ type transition dominates. For the same reason the competing $4^+ \to 0^+$ transition (type $E4$) is strongly hindered compared to the $E2$ type

[1] Apart from a small recoil correction, which is negligible compared to typical energy resolution of modern γ-ray detectors.

Table 2.1: Selection rules for the type of γ-ray transition

Multipolarity	Dipole		Quadrupole		Octupole		...
Parity change	Yes	No	No	Yes	Yes	No	...
Type of transition	E1	M1	E2	M2	E3	M3	...

transition.

The transition probability for γ decay can be expressed as

$$\lambda(\sigma L) = \frac{2(L+1)}{\varepsilon_0 \hbar L \left[(2L+1)!!\right]^2} \left(\frac{E_\gamma}{\hbar c}\right)^{2L+1} B(\sigma L), \tag{2.14}$$

where $B(\sigma L)$ is the *reduced transition probability*, and σ stands for the electric or magnetic character of the transition. Calculation of $B(\sigma L)$ requires information of the nuclear wave function, and it can be very challenging. However, an estimate can be obtained for the $B(\sigma L)$ by assuming a single proton transition between two states of the spherical shell model. These estimates are often called *Weisskopf estimates* or *single particle estimates*, and they are listed in table 2.2 for the most common transition types. These estimates are obviously quite rough, but they are often used as a comparison for experimental observations. The ratio $T_{1/2}^{Weisskopf}/T_{1/2}^{experimental}$ for the partial half-lifes of γ-decay is usually given in *Weisskopf units* (W.u.).

Moreover, for the case when an initial state I decays through $M1$ and $E2$ type transitions to states $I-1$ and $I-2$, respectively, from experimental data it is straightforward to calculate the reduced transition strength ratio

$$\frac{B(M1)}{B(E2)} = 0.697 \frac{E_\gamma(E2)^5 I_\gamma(M1)}{E_\gamma(M1)^3 I_\gamma(E2)(1+\delta^2)} \left[\frac{\mu_N^2}{(eb)^2}\right]. \tag{2.15}$$

Here I_γ refers to the γ-ray intensity, and $\delta^2 = {}^{I_\gamma(M1)}/_{I_\gamma(E2)}$ [Morinaga76] is the mixing ratio for the $M1$ type transition competing with the non-stretched $E2$ transition. For simplicity the transitions have been assumed to be pure in

Table 2.2: Weisskopf estimates. E_γ must be given in units of MeV. Numerical factors may vary in the literature, these are taken from [Suhonen07].

σL	λ [$1/s$]	σL	λ [$1/s$]
$E1$	$1.023 \cdot 10^{14} E_\gamma^3 A^{2/3}$	$M1$	$3.184 \cdot 10^{13} E_\gamma^3$
$E2$	$7.265 \cdot 10^{7} E_\gamma^5 A^{4/3}$	$M2$	$2.262 \cdot 10^{7} E_\gamma^5 A^{2/3}$
$E3$	$3.385 \cdot 10^{1} E_\gamma^7 A^{2}$	$M3$	$1.054 \cdot 10^{1} E_\gamma^7 A^{4/3}$

this work. Transition energies E_γ must be introduced in units of MeV. The equation 2.15 can be extracted by solving $B(\sigma L)$ from the equation 2.14.

2.6.2 Internal conversion

Internal conversion is a competing phenomenon for the depopulation of an excited state through γ-ray transitions. In the process of internal conversion the nucleus changes a virtual γ-ray with one of the atomic electrons in one of the electron shells. Consequently the electron is emitted, and the exited state is depopulated. Internal conversion always leaves a vacancy in the electron shell, which is promptly filled by one of the electrons in higher orbitals. This leads to the emission of an x-ray, or an Auger electron. The energy of the conversion electron is $E_{e^-} = E_\gamma - B_{e^-}$, where B_{e^-} is the binding energy of the electron, and the E_γ is the energy difference between initial and final states of the nucleus. Electrons from different atomic orbitals will appear with different energies due to different binding energies. These are usually referred as a K-conversion, L-conversion and so on depending on the origin of the electron. The *Internal conversion coefficient* α is defined as the fraction of the internal conversion

$$\alpha = \frac{\lambda_{e^-}}{\lambda_\gamma}. \tag{2.16}$$

Moreover, the internal conversion coefficient can be defined separately for each atomic shell, but the total internal conversion coefficient is the sum of all sub-coefficients

$$\alpha = \alpha_{\mathrm{K}} + \alpha_{\mathrm{L}} + \alpha_{\mathrm{M}} + \dots . \tag{2.17}$$

Typically the heavier the nucleus or lower the transition energy or higher the transition multipolarity, the higher the internal conversion branch. Internal conversion offers an effective probe for determining the type of transition. In the case of our experimental setup, the resolution of a typical silicon-based particle detector is enough to separate K-conversion, but other conversion types are observed in one peak. However, determining the intensity ratio $^{K}/_{L+M+\dots}$ from experimental data and comparing that to the theoretical (see for example [Kibédi08]) value is usually enough to separate different transition types from each other. In addition by using equation 2.16 one may determine the *transition intensity* as a sum of *γ-ray intensity* and *internal conversion intensity*:

$$I_{\mathrm{TR}} = I_{\gamma} + I_{\mathrm{e}^-} = I_{\gamma}(1 + \alpha). \tag{2.18}$$

As stated earlier, photons cannot have zero angular momentum. However, the transition between two 0^+ states itself is not forbidden. These $E0$ type transitions proceed solely by internal conversion.

Chapter 3

Experimental Methods

This experimental work was carried out using *fusion evaporation reactions*. The experimental setup used in this study is presented in Fig. 3.1. The setup consists of three main pieces of equipment. Around the target position there is the JUROGAM II array of Compton-suppressed high-purity germanium detectors, which is used to detect prompt γ rays at the target position. Fusion evaporation residues, later called recoils, were separated from the primary beam in the gas-filled recoil separator RITU. At the focal plane of RITU the recoils were then studied using the GREAT spectrometer. This chapter introduces the experimental setup used in this study.

3.1 Fusion-evaporation reactions

One possible way of producing exotic nuclei is to use fusion evaporation reactions. In this type of reactions typically a medium heavy or heavy target (t) foil is radiated with a light or a medium heavy beam (b). In the reaction the beam and target nuclei may get close enough and fuse together forming a heavy or superheavy compound nucleus. This is illustrated in Fig. 3.2(a). The minimum beam energy required for the fusion is set by the Coulomb barrier B_C between the target and the beam nucleus:

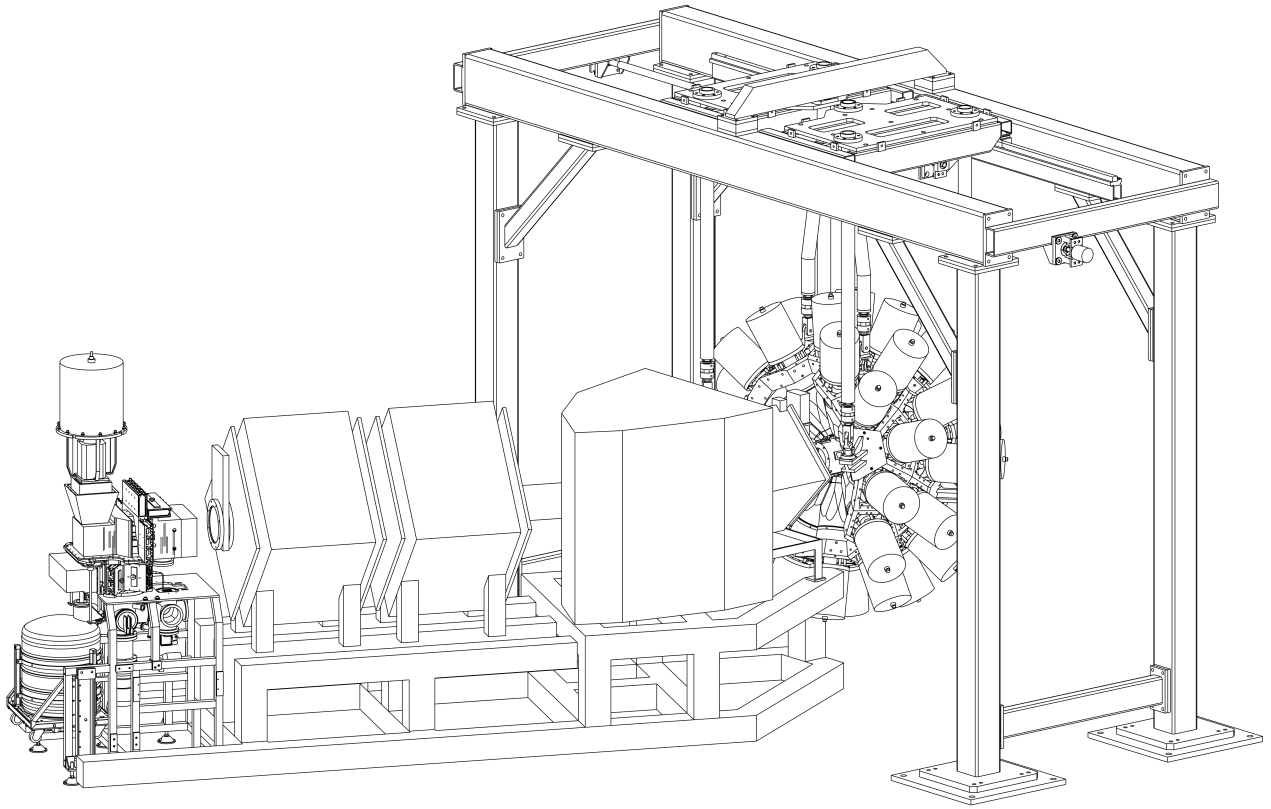

Figure 3.1: The experimental setup used in this study. The spherical object on the right hand side of the figure is the JUROGAM II array of Compton-shielded high-purity germanium detectors. It is used to observe prompt γ rays at the target position. In the middle there is the gas-filled recoil separator RITU that is used to separate fusion-evaporation residues from the primary beam. On the left hand side of the figure there is the GREAT spectrometer used to study the decay of evaporation residues, and isomeric states in them. Figure courtesy of Dave Seddon (Liverpool NSG).

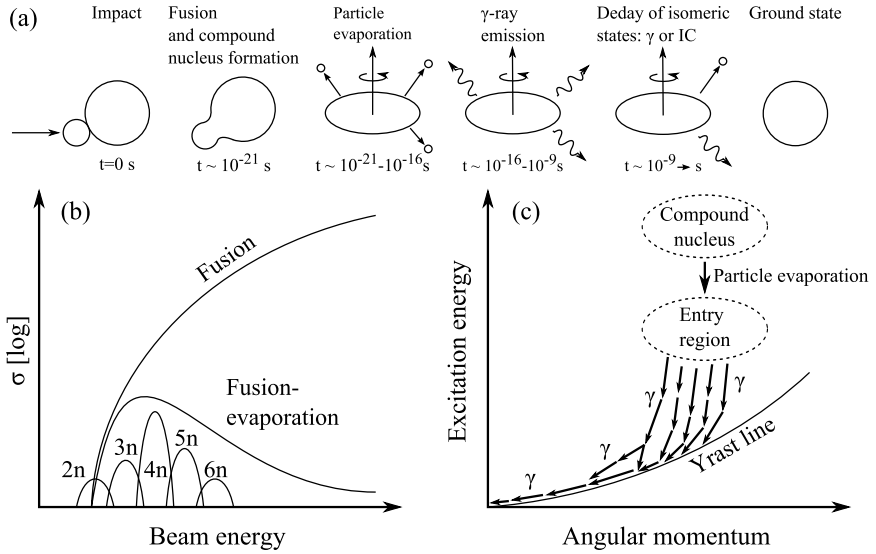

Figure 3.2: (a) Schematic progress of a fusion-evaporation reaction. (b) Schematic cross sections for different fusion evaporation channels as a function of beam energy. Only neutron evaporation channels are shown, but also charged particle (proton, α-particle) evaporation may occur. (c) Schematic depopulation of excited states in a typical fusion evaporation reaction.

$$B_C \approx 1.44\ \text{MeV} \cdot \text{fm} \frac{Z_\text{b} \cdot Z_\text{t}}{r_\text{b} + r_\text{t}}, \tag{3.1}$$

where $r = r_0 A^{1/3}$ is the radius of the respective nucleus. The value of the radius parameter r_0 varies, but is typically ~ 1.4 fm in this mass region. Immediately after fusion the compound nucleus is in a highly excited (Fig. 3.2(c)) state E^*,

$$E^* = E_\text{CM} + Q, \tag{3.2}$$

where Q is the reaction energy[1] and E_CM is the kinetic energy of the system in center of mass frame:

[1]The Q-value for any reaction or decay is defined as the mass difference between initial and final particles.

$$E_{\mathrm{CM}} = \frac{m_{\mathrm{t}}}{m_{\mathrm{t}} + m_{\mathrm{b}}} E_{\mathrm{LAB}}. \tag{3.3}$$

In the region of the nuclear chart where the nuclei of this study are located, the compound nucleus is likely to undergo fission. However, there is a small chance that the excitation energy is released through particle evaporation. Typically some neutrons are emitted, but also protons and α-particles or some combination of these may be emitted, within the limits of the excitation energy. The production rate R for different evaporation channels is set by the cross section σ of each channel:

$$R = N\sigma\Phi, \tag{3.4}$$

where N is the number of target nuclei exposed to beam flux Φ. Schematic cross sections for neutron-evaporation channels are presented in Fig. 3.2(b). This figure does not show the charged particle evaporation channels for graphical reasons, but typically the $p(x-1)n$ channel roughly overlaps in energy with the xn evaporation channel. Excitation functions for each evaporation channel are sharp, hence the beam energy (excitation energy) must be chosen carefully, in order to maximize the production of the nucleus under study.

The fusion-evaporation reactions used in this study were ^{165}Ho(^{40}Ar,4n)^{201}At and ^{165}Ho(^{40}Ar,6n)^{199}At. The thickness of the self supporting ^{165}Ho target was 350 $\mu g/cm^2$. Beam energies of 172 MeV and 205 MeV (LAB), average beam intensities of 11 pnA and 9 pnA, and irradiation times of 83 h and 130 h were used in the production of ^{201}At and ^{199}At, respectively. These beam energies are high enough to allow fusion reactions, because the Coulomb barrier[1] in these reactions is around 170 MeV (LAB). The beam energies correspond to excitation energies[1] of 51.5 MeV and 78.0 MeV for the compound nuclei, respectively. Relative production yields for the nuclei under study can be estimated from the α-particle energy spectrum presented in Fig. 3.3. The absolute cross sections were estimated to be $\sim$ 160 μb and $\sim$ 1 mb for ^{199,201}At, respectively.

[1]Calculated with the PACE4 code in LISE++ framework.

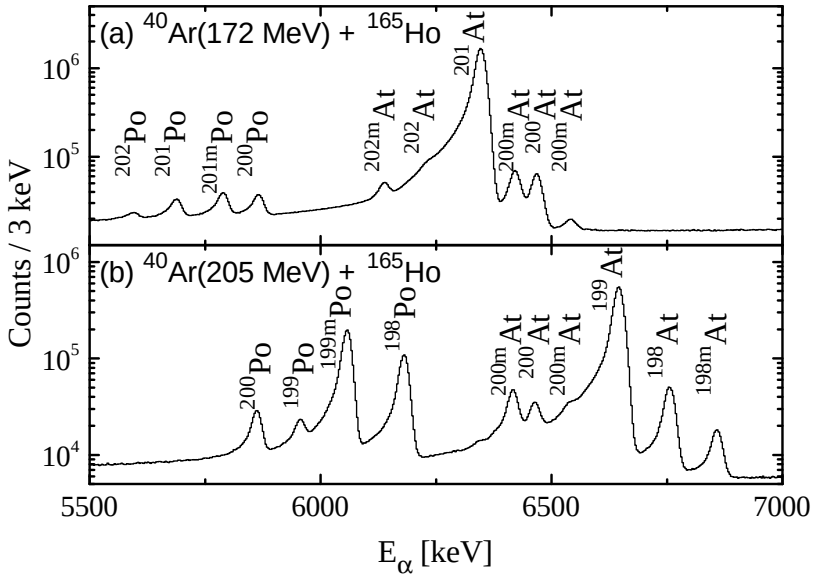

Figure 3.3: Raw α-particle energy spectrum obtained with the reactions used in this study. The figure is from [Auranen14].

3.2 Gas-filled recoil separator RITU

The beam intensity in a typical fusion-evaporation experiment is in the order of $10^{10} \ldots 10^{13}$ particles per second to the target. Nuclear reactions occur rarely, so effectively the same intensity proceeds through the target. However, any silicon detector would be almost immediately destroyed, if exposed to such a particle flux. Therefore it is essential to get rid of the primary beam after the target. This separation is possible due to different magnetic rigidities $B\rho$ of the beam and the recoils when a magnetic dipole is operated in gas-filled mode. The magnetic rigidity of an ion can be expressed as follows:

$$B\rho = \frac{\sqrt{2Em}}{q}, \tag{3.5}$$

where E, m and q represent the kinetic energy, mass and charge of the ion, respectively.

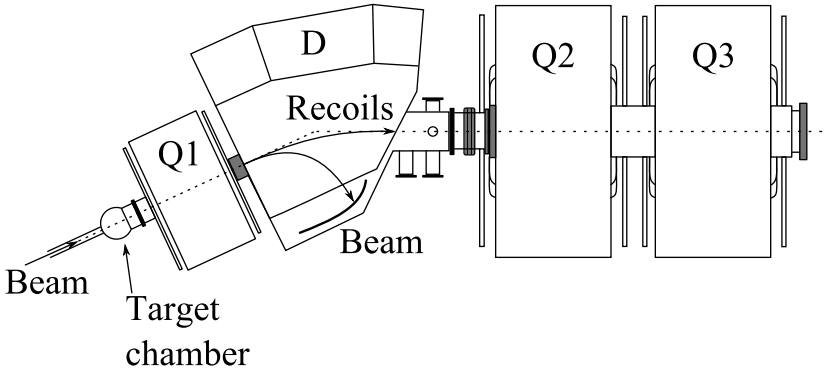

Figure 3.4: Gas-filled recoil separator RITU. Q represents a focusing quadrupole magnet, and D represents a separating dipole magnet. RITU is typically filled with $\sim$ 1 mbar of helium.

The separator used in this experiment is called the Recoil Ion Transport Unit, RITU [Leino95, Sarén11], and it is shown in Fig. 3.4. It is a gas-filled recoil-separator with ion optical configuration of QDQQ. After the target there is a vertically focusing quadrupole (Q) magnet to maximize the dipole acceptance, followed by a separating dipole (D) magnet. After the dipole there are two more quadrupole magnets, one horizontally and one vertically focusing. The idea of the gas filling is to maximize the collection of different charge states. After the fusion evaporation the recoils have a large charge state distribution. While the recoils fly through RITU, they change their charge state several times in the collisions with the medium gas. Therefore the recoils follow a path of the average charge state, and the initial charge state becomes meaningless.

3.3 GREAT spectrometer

After the RITU separator the recoils are guided to the GREAT spectrometer [Page03]. The schematic layout of GREAT is presented in Fig. 3.5(a). Before implantation into the double-sided silicon strip detector (DSSD) the recoils pass through a multi-wire proportional counter (MWPC). The DSSD consists of two 300-µm thick silicon detectors both with a size of 40 mm$\times$60 mm with a strip width of 1 mm. The DSSD can also be used to detect charged particles

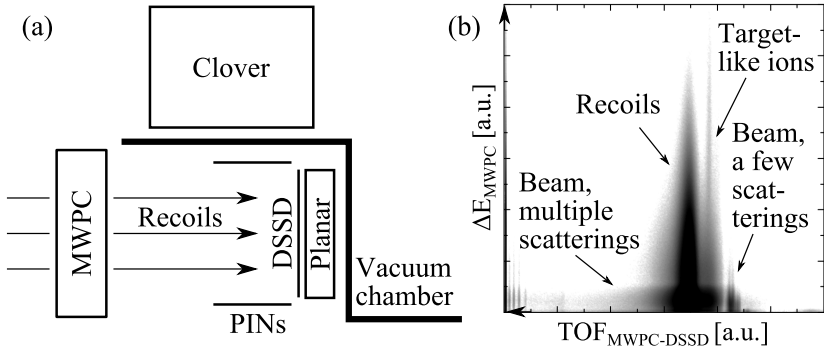

Figure 3.5: (a) Schematic layout of the detectors in the GREAT spectrometer. Two side clovers are omitted for visual purposes. (b) Energy loss of ions in the MWPC as a function of the MWCP-DSSD Time-Of-Flight. Note that the values of TOF grows to the left. Setting a proper 2D-gate to this matrix allows recoil gating.

originating from the decay of an isomeric state or the ground state of the recoil. In this experiment the horizontal strips were set to measure recoil and α-particle energies, and the vertical strips were set to measure conversion electron energies. Due to the implantation of the recoils, the DSSD works as a calorimetric detector. Because of this, the observed energies of the K-conversion electrons are $\sim$12 keV higher than the actual electron energy due to the relaxation (low-energy x-rays, Auger electrons) of the electron cloud. For the same reason the measured $L + M + \ldots$-conversion electron energies correspond to the full transition energy. The DSSD is surrounded by 28 PIN silicon diodes in a box arrangement. In this work these detectors were used to detect escaped conversion electrons from the DSSD, but also α-particles are observable. Four germanium detectors in close geometry around the DSSD were used to detect γ rays. A planar detector is placed immediately behind the DSSD, and it has a large efficiency for low-energy γ rays. Outsize of the vacuum chamber there are three clover type detectors, that were used to detect both low- and high-energy γ rays. For higher efficiency, the clover on top of the GREAT vacuum chamber is bigger than the two side clovers.

The MWPC is needed in order to distinguish between recoils and unwanted ions. As the typical beam intensity is high in our experiments, there are always some beam particles that end up after (multiple) scattering to the

DSSD. Scattered beam particles are lighter than the real recoils, hence their energy loss in the MWPC is smaller, and the time-of-flight between the MWPC and the DSSD is shorter. This is illustrated in Fig. 3.5(b). The scattered target-like ions can be also separated from recoils with this method. The MWPC is normally used as a veto detector for the DSSD to distinguish decay events from implanted recoils and scattered beam particles.

Calibration of the focal plane clover detectors were performed by using standard ^{152}Eu and ^{133}Ba γ-ray sources. The shape of the relative efficiency curve of the focal plane clovers is identical to JUROGAM II array clovers (see rings 3 and 4 in Fig. 3.7). The planar detector has a large efficiency for low-energy γ-rays when compared to clover detectors. The calibration of the PIN diodes was done with a 3-line α source (containing ^{239}Pu, ^{241}Am and ^{244}Cm) and conversion electrons from a ^{133}Ba source. Also the DSSD x-side was calibrated with the ^{133}Ba conversion electron source. The DSSD y-side was at first rough-calibrated with the 3-line α source for the on-line analysis, and later in the off-line analysis an internal calibration was introduced.

3.4 JUROGAM II array

Figure 3.6 presents the JUROGAM II array of Compton-suppressed high-purity germanium detectors, which is used to detect prompt γ rays around the target position. The array consists of 24 Clover type detectors [Duchêne99], and altogether 15 Phase1 [Beausang92] and GASP [Alvarez93] type detectors. Each detector is placed inside a BGO (Bismuth Germanate) scintillator detector for Compton suppression. The detectors are grouped into four rings with respect to the beam line. Rings one and two consist of Phase1 and GASP type detectors, and rings three and four consist of clover type detectors. The angle between beam axis and each ring is marked in the Fig. 3.6. After the fusion evaporation the recoil typically flies with a speed of $\sim$ 2 % of the speed of light. Therefore it is necessary to apply the Doppler correction to the observed γ-ray energy:

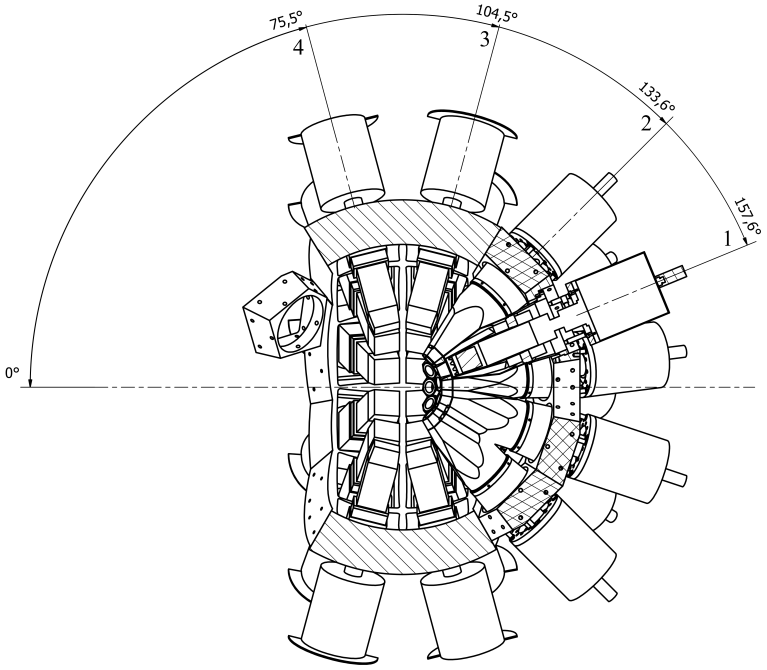

Figure 3.6: JUROGAM II array of high-purity germanium detectors. JUROGAM II consists of two rings (rings 1 and 2) of Phase1 and GASP type detectors and two rings (rings 3 and 4) of clover type detectors. Each detector is placed inside a BGO Compton shield. The beam enters from the right, and the horizontal dashed line represents the beam line. The target is at the middle of JUROGAM II, and RITU is on the left hand side of the figure.

$$E_\gamma = \frac{E_0\sqrt{1-\beta^2}}{1-\beta\cos\theta}, \tag{3.6}$$

where E_0 is the observed γ-ray energy, $\beta = v/c$ is the speed of the recoil with respect to the speed of light, and θ is the angle of the detector with respect to the recoil velocity vector. The Doppler effect causes also a broadening of the observed γ-ray energy distribution. Using a stationary calibration source a resolution (FWHM) of $\sim$2.3 keV was obtained for a 302-keV γ-ray transition, whereas a resolution of $\sim$3.1 keV was achieved for a 296-keV transition from the in-beam data.

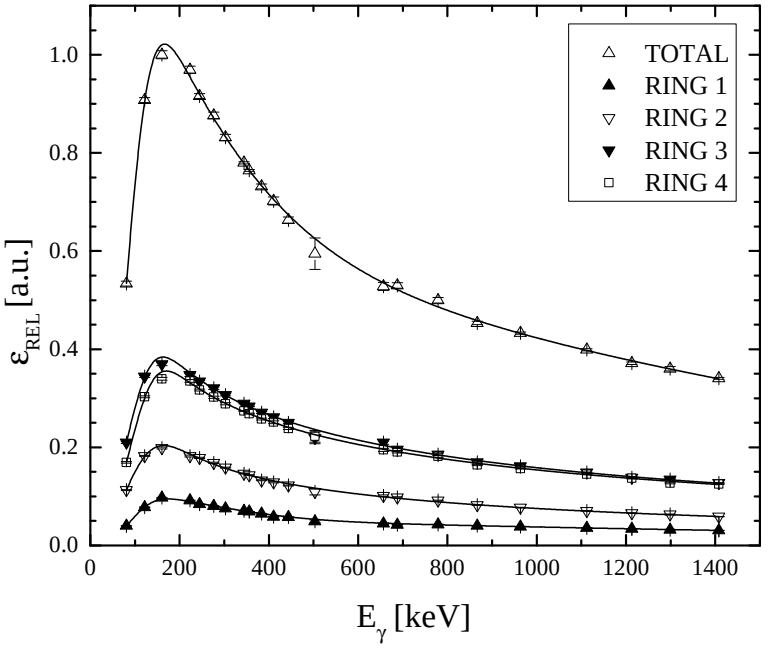

Figure 3.7: Relative efficiency of the JUROGAM II array obtained from europium barium source data. The total efficiency is compared to the efficiency of each ring. Solid lines represent a fit to the source data. The curves are normalized such that the data point with highest efficiency for the whole array is unity.

Energy and efficiency calibrations for the JUROGAM II array were performed by using standard radiation sources. A source containing a mixture of ^{152}Eu and ^{133}Ba was selected for this purpose. The obtained relative efficiency curves using the add-back[1] procedure are presented as a function of γ-ray energy in Fig. 3.7. It is worth noting the minor difference between the two clover rings for small energy γ rays. The rings are identical, but the target holder partially shadows the ring four, hence the efficiency of ring four is slightly less than the efficiency of ring three.

Angular distributions of γ rays originating from prompt transitions can be used in the deduction of the transition multipolarity. Immediately after fusion

[1]If there is a Compton scattering between two neighboring non diagonal clover crystals, these events can be reconstructed in the add-back process.

the rotation axis of a nucleus is perpendicular with respect to the beam axis. In this case the angular distribution of γ rays follows the distribution function [Mateosian74]

$$W(\theta) = 1 + \alpha_2 A_2^{\max} P_2(\cos(\theta)) + \alpha_4 A_4^{\max} P_4(\cos(\theta)), \tag{3.7}$$

where A stands for the angular distribution coefficient, α is the respective attenuation coefficient and P is a Legendre polynomial. Usually a simplification is made by setting A_4 to zero, which is equal to ignoring multipole mixing. This leads to the first order approximation

$$W(\theta) = A_0 \left[1 + A_2 P_2(\cos(\theta))\right], \tag{3.8}$$

that is useful in determination of transition multipolarities. Here a positive A_2 coefficient indicates a stretched quadrupole character, while a negative value indicates a stretched dipole character. Some examples of angular distribution analysis are presented in Fig. 3.8. An alternative method is to calculate intensity ratios

$$R_1 = \frac{I_\gamma(133.6^\circ) + I_\gamma(157.6^\circ)}{I_\gamma(104.5^\circ)} \;\&\; R_2 = \frac{I_\gamma(133.6^\circ) + I_\gamma(157.6^\circ)}{I_\gamma(75.5^\circ)}, \tag{3.9}$$

where values of $R = 1.30(7)$ and $R = 0.70(6)$ [Ruotsalainen13] stand for stretched quadrupole and dipole transitions, respectively. It is worth noting that the method described is not able to distinguish unambiguously between either a $\Delta I = 0$ dipole and a stretched $E2$ transition or stretched dipole and unstretched/mixed $E2$ transitions. Both methods described above were confirmed by comparing observed angular distributions and ratios to transition types of previously known transitions.

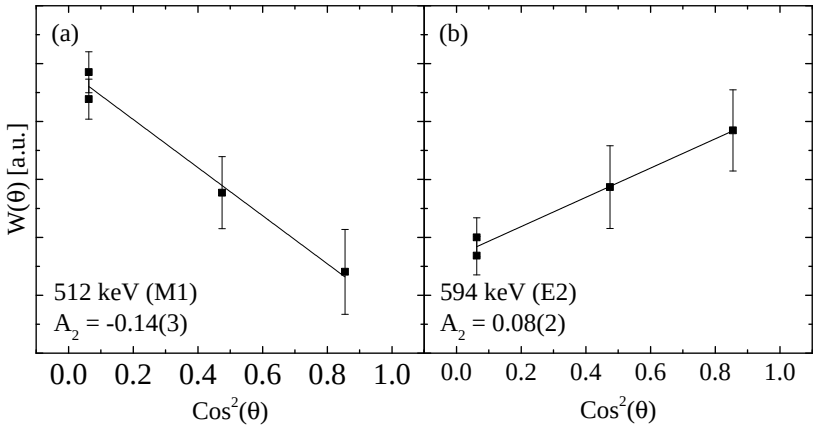

Figure 3.8: Two examples of angular distributions of γ rays observed in JUROGAM II. A positive A_2 indicates a stretched quadrupole character, while a negative value indicates a stretched dipole character. Detector rings three and four are symmetric around $\theta = 90°$, hence the two left-most data points always overlap.

3.5 Data acquisition and -analysis

Data from all data channels were recorded independently using the triggerless total data readout method (TDR) [Lazarus01]. An absolute time stamp was given for each event by a 100-MHz clock, corresponding to 10 ns time resolution. All focal-plane events were recorded together with the recoil-tagged JUROGAM II events. The data can be sorted afterwards by demanding a certain chain of events to occur. All of the data analysis and sorting were performed by using the GRAIN software [Rahkila08]. GRAIN allows a large variety of different tagging and gating techniques to be used in the sorting of the data. The most simple gating technique used is recoil gating. In this method only those prompt γ rays that are associated with a recoil, identified by the method presented in Fig. 3.5(b) and the associated text, are accepted. A subset of the previous γ-rays can be selected by demanding a decay event of the recoil occuring within a certain time window in the same pixel of the DSSD into which the recoil was implanted. The time window between the recoil implantation and decay is often chosen to be roughly three times the half-life of the decay. This search time corresponds to a probability of less

than 13 % for losing the event due to the finite search time. This tagging technique is called recoil-decay tagging. The decay itself can be any form of nuclear decay, such as α decay, or internal conversion decay of an isomeric state. In the case of an isomeric γ decay the pixel condition cannot be used. This method is then limited to short half-lives. A large variety of different tagging methods was used in this work, and the details of the methods used are given in chapter 4 when each method is implemented.

Chapter 4

Results

This chapter summarizes the experimental observations and justifications for the conclusions made in this work. Next the results will be presented one subject at a time.

4.1 Isomeric $^{29}/_{2}^{+}$ state in ^{201}At and subsequent levels

Figure 4.1(a) shows the recoil gated γ-ray singles energy spectrum observed in JUROGAM II using the reaction ^{165}Ho(^{40}Ar,4n)^{201}At. Figure 4.1(b) shows the energy spectrum of delayed γ rays observed in the GREAT clover array within 14 μs of the recoil implantation using the same reaction. This time window corresponds roughly to four times the half-life of the isomeric state under study, and the same search time is applied to all delayed γ-ray energy spectra presented in this section. The deduction of the half-life will be presented at the end of this section. When comparing these two spectra two findings can be identified: Firstly, several identical γ-ray transitions can be identified in both spectra, some of which have been identified earlier [Dybdal83]. Secondly, the 269- and 339-keV transitions are missing from the prompt spectrum. These two findings hint that there is a high-lying isomeric state in ^{201}At, that is

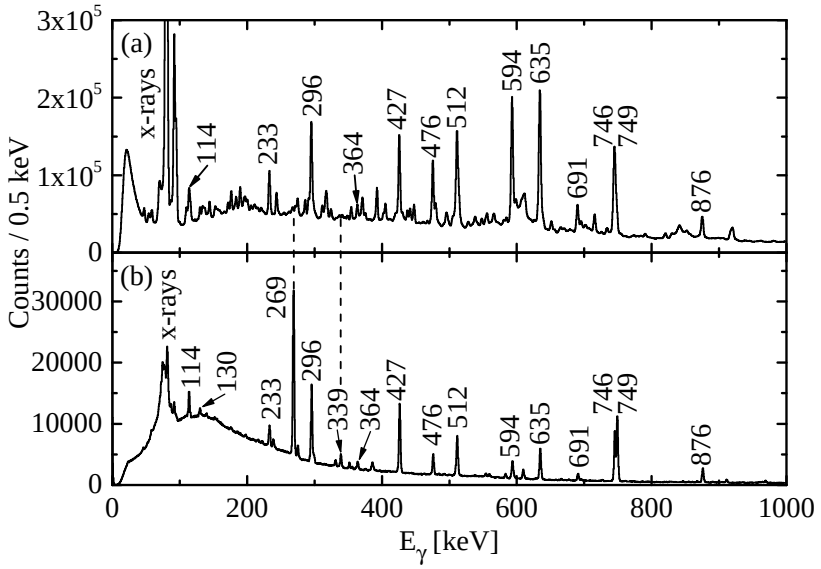

Figure 4.1: (a) Energy spectrum of recoil gated γ rays observed in JUROGAM II. (b) Energy spectrum of γ rays observed in the focal plane clover array within 14 μs from the recoil implantation

depopulated through the 269- and 339-keV γ-ray transitions.

Figure 4.2 presents a few examples of the focal plane clover $\gamma\gamma$ coincidence data. In panel (a) the energy spectrum of γ rays in coincidence with the 269-keV transition is shown. The 427-, 746- and 749-keV transitions have previously been assigned to the positive parity band of ^{201}At [Dybdal83], hence the 269-keV transition mainly feeds the positive parity band. Panel (b) shows the energy spectrum of those γ rays, which are in prompt coincidence with either the 476- or the 594-keV transition. The 476-, 594-, and 635-keV transitions have earlier been assigned to the negative parity band [Dybdal83], hence the 339-keV transition feeds the negative parity cascade.

In addition to the transitions observed in clover spectra, there are a few low-energy γ-ray transitions that are only visible in the planar detector. Figure 4.3(a) shows the energy spectrum of γ rays obtained using the planar detector in coincidence with the 269-keV γ ray observed in the focal plane clover array. It is worth noting the deviant K_α/K_β x-ray intensity ratio. This suggests that

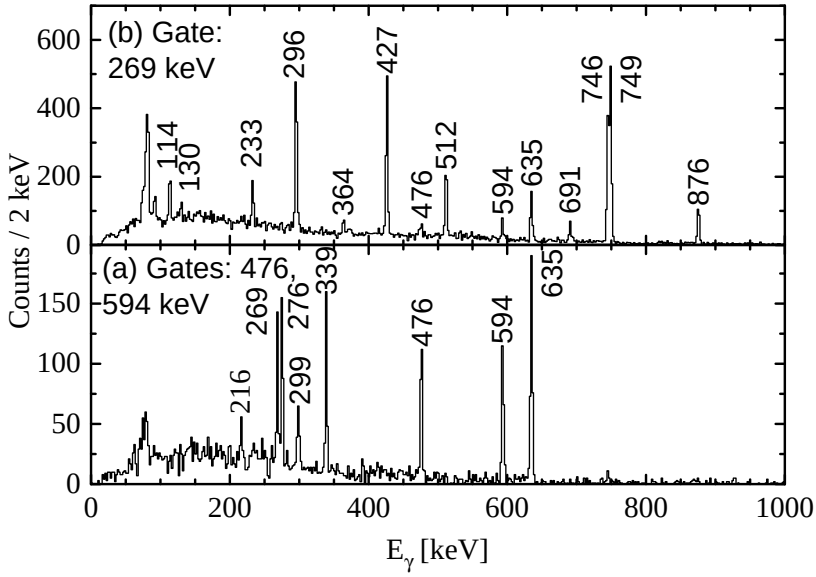

Figure 4.2: Recoil gated delayed $\gamma\gamma$ energy spectra observed in the GREAT clover array: (a) Energy spectrum of γ rays in coincidence with the 269-keV γ ray. (b) Energy spectrum of γ rays in coincidence with the 476- or 594-keV γ ray.

there is a γ-ray transition in the positive parity cascade with a transition energy similar to the K_α x-ray energy.

The observed γ rays depopulating the $^{29}/_{2}^{+}$ isomeric state are listed in table 4.1. The level scheme below the isomeric state was built based on the $\gamma\gamma$ coincidence information, multipolarity information, and energy sum arguments. The validity of the level scheme was verified by calculating the transition intensities at the focal plane $I_{\mathrm{TR}}(FP)$ for each transition. The transition intensities are also listed in table 4.1. The internal conversion coefficients needed to calculate the $I_{\mathrm{TR}}(FP)$ were taken from the BrIcc [Kibédi08]. The deduced level scheme is presented in Fig. 4.4.

The major branch of the depopulation of the $^{29}/_{2}^{+}$ state goes through the 269-keV $E2$ transition, but there is also a depopulating 339-keV $E3$ transition that has been observed. These transition type assignments were confirmed by the $^{K}/_{L+M+\ldots}$ internal conversion intensity ratio observed in the PIN diodes.

Table 4.1: Observed γ rays following the decay of the $^{29}/_{2}^{+}$ isomeric state in ^{201}At. I_γ is the relative γ-ray intensity and A_2 is the angular distribution parameter, both are deduced from JUROGAM II data. The γ-ray energies E_γ and intensities I_γ as well as the transition intensities at the focal plane $I_{\mathrm{TR}}(FP)$ are deduced from the focal plane clover data, if not specified. Internal-conversion coefficients for the calculation of $I_{\mathrm{TR}}(FP)$ were taken from [Kibédi08]. $I_{\mathrm{TR}}(FP)$ is normalized such that the 269-keV γ-transition has an intensity of 100.

E_γ [keV]	I_γ	A_2[1]	I_γ(FP)	I_{TR}(FP)	$I_{\mathrm{i}}^{\pi}[\hbar]$	$I_{\mathrm{f}}^{\pi}[\hbar]$
46.5(2)[2]			3.9(12)[2]	90(30)[2]	$^{25}/_{2}^{+}$	$^{23}/_{2}^{+}$
58.5(2)[2]			4.3(13)[2]	6(2)[2]	$^{13}/_{2}^{+}$	$^{11}/_{2}^{-}$
83.0(4)[3]			23(8)[4]	120(40)[4]	$^{23}/_{2}^{+}$	$^{21}/_{2}^{+}$
114.1(2)			9.2(12)	12(2)	$^{13}/_{2}^{+}$	$^{13}/_{2}^{-}$
130.3(2)	3.9(4)	-0.36(7)	3.0(5)	20(3)	$^{17}/_{2}^{+}$	$^{17}/_{2}^{+}$
216.3(3)			1.2(3)	1.3(3)	$^{21}/_{2}^{+}$	$^{21}/_{2}^{-}$
233.4(2)	14.5(4)	-0.05(2)	11.6(14)	24(3)	$^{17}/_{2}^{+}$	$^{15}/_{2}^{+}$
269.0(2)			100(10)	118(11)	$^{29}/_{2}^{+}$	$^{25}/_{2}^{+}$
275.5(2)	6.6(2)	-0.47(2)	7.0(9)	12(2)	$^{23}/_{2}^{-}$	$^{21}/_{2}^{-}$
295.9(2)	40(2)	0.11(4)	51(5)	60(6)	$^{21}/_{2}^{+}$	$^{17}/_{2}^{+}$
299.3(2)			4.9(7)	5.0(7)	$^{23}/_{2}^{+}$	$^{21}/_{2}^{-}$
339.2(2)			9.8(9)	14(2)	$^{29}/_{2}^{+}$	$^{23}/_{2}^{-}$
364.1(3)	6.5(3)	-0.11(3)	6.4(11)	8(2)	$^{17}/_{2}^{+}$	$^{15}/_{2}^{+}$
426.5(2)	39(2)	0.14(7)	66(8)	69(9)	$^{21}/_{2}^{+}$	$^{17}/_{2}^{+}$
476.2(2)	33(1)	0.13(4)	20(4)	21(4)	$^{21}/_{2}^{-}$	$^{17}/_{2}^{-}$
511.8(2)		-0.14(3)	34(6)[5]	38(7)[5]	$^{15}/_{2}^{+}$	$^{13}/_{2}^{+}$
593.8(2)	77(3)	0.08(2)	24(4)	25(4)	$^{17}/_{2}^{-}$	$^{13}/_{2}^{-}$
635.1(2)	100(3)	0.09(4)	41(6)	42(6)	$^{13}/_{2}^{-}$	$^{9}/_{2}^{-}$
691.1(2)			9.9(13)	11(2)	$^{11}/_{2}^{-}$	$^{9}/_{2}^{-}$
745.5(2)	74(2)	0.4(2)	71(8)	72(8)	$^{17}/_{2}^{+}$	$^{13}/_{2}^{+}$
749.3(2)			94(11)	105(12)	$^{13}/_{2}^{+}$	$^{9}/_{2}^{-}$
876.1(2)	19.4(6)	0.16(3)	24(3)	24(3)	$^{17}/_{2}^{+}$	$^{13}/_{2}^{+}$

[1]See equation 3.8.

[2]Deduced from the recoil-gated planar singles spectrum.

[3]Calculated from the assumption that in a closed loop of transitions the energy shift is zero. Two loops were used, the weighted average of the results is presented.

[4]Deduced from the 746- or 749-keV gated planar vs. clover γ-γ data. The number of K_α x-rays is subtracted based on the number of observed K_β x-rays.

[5]Deduced from 296-keV gated focal plane clover $\gamma\gamma$ data.

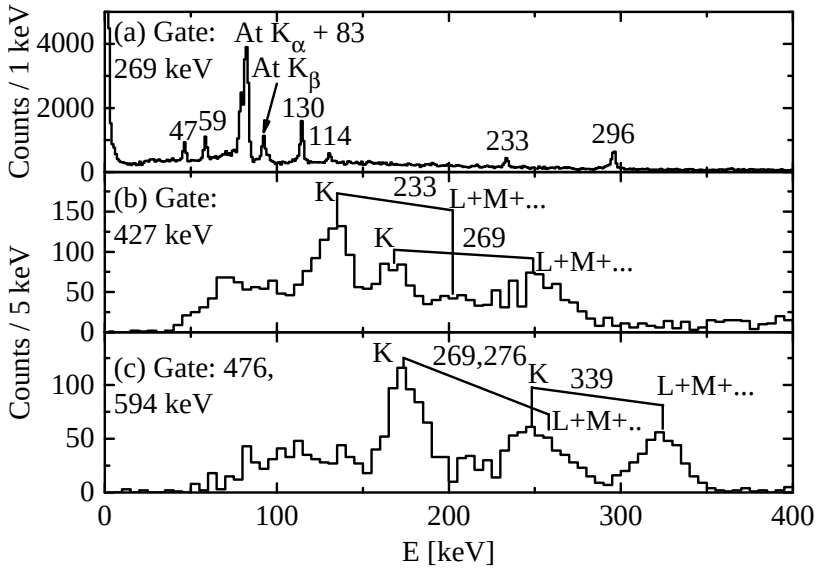

Figure 4.3: (a) Energy spectrum of γ rays observed in planar detector in prompt coincidence with the 269-keV γ-ray transition observed in clover array. Conversion-electron energy spectra obtained using PIN diodes: (b) energy spectrum of conversion electrons in coincidence with the 427-keV γ ray observed in focal plane clover array. (c) energy spectrum of conversion electrons in coincidence with the 476- or 594-keV γ ray observed in focal plane clover array.

These spectra are shown in Fig. 4.3(b) and (c). In the case of the 269-keV transition the observed $^{K}/_{L+M+...}$ intensity ratio of 0.93(5) matches well with the theoretical value of 0.89(2) [Kibédi08] calculated for a 269-keV $E2$ transition. The 339-keV K-conversion overlaps with the $L + M + \ldots$-conversions of the 269- and 276-keV transitions. Because of this, the number of 269- and 276-keV $L + M + \ldots$-conversion events was subtracted from the $\sim$250-keV peak. This was based on the $^{I_\gamma(269)}/_{I_\gamma(276)}$ intensity ratio obtained from the spectrum shown in Fig. 4.2(b), the number of observed K-conversion events for 269- and 276-keV transitions, and theoretical $^{K}/_{L+M+...}$ intensity ratios for the 269-keV $E2$ and 276-keV $M1$ transitions. The residual events in the $\sim$250-keV peak belong to the 339-keV K-conversion. This method yields an intensity ratio $^{K}/_{L+M+...}$ =0.45(4), which matches well with the value of 0.416(8) calculated for a 339-keV $E3$ transition.

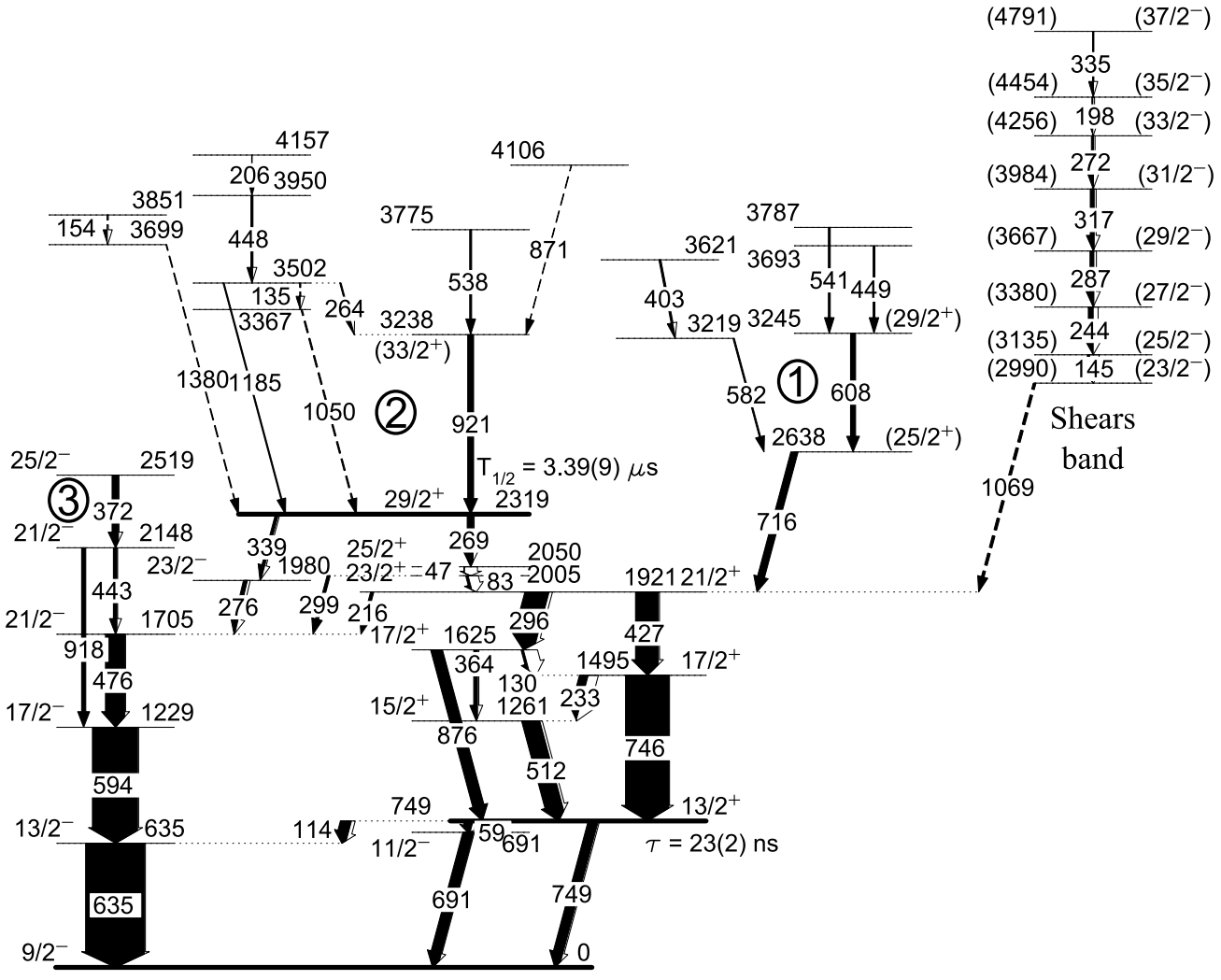

Figure 4.4: Partial level scheme of ^{201}At. Levels associated with the isomeric $^{1}/_{2}^{+}$ state are presented in Fig. 4.6(b). The circled number indicates a numerical label used to categorize transitions. The mean life-time of the $^{13}/_{2}^{+}$ state is taken from [Dybdal83], rest of the information is from this experiment. The figure is from [Auranen15].

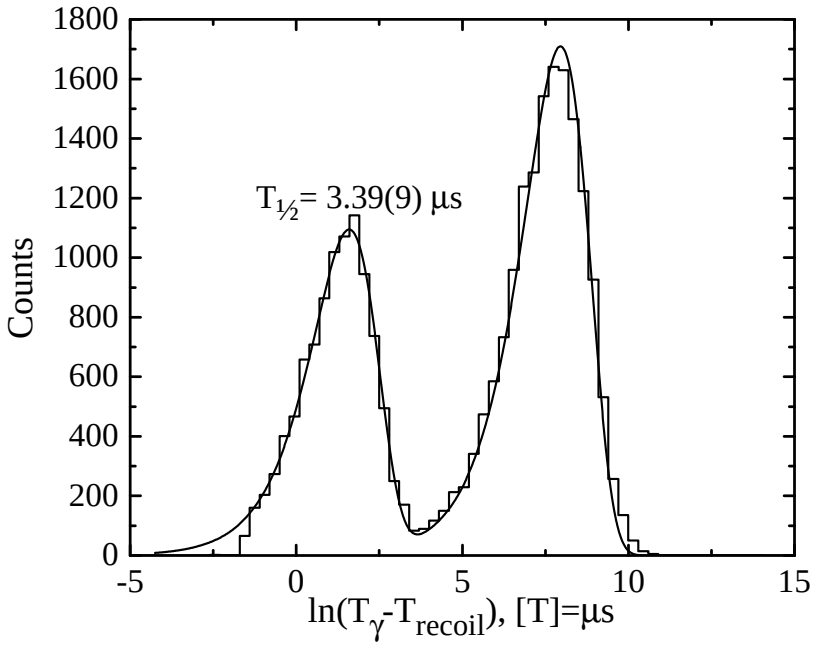

Figure 4.5: Time distribution between the recoil implantation and the following 269-keV γ ray observed in the planar detector. Prompt coincidence with the 296-, 427-, 594-, 635-, 746-, or 749-keV, γ ray was demanded in the focal plane clover array. The logarithmic time-scale method [Schmidt00] suggests a half-life of $3.39(9)$ μs. The longer living component is a result from random γ-ray coincidences, originating for example from Compton scattering. The figure is from [Auranen15].

The time distribution between recoil implantation and the subsequent 269-keV γ ray observed in the planar detector is shown in the Fig. 4.5. In addition the 296-, 427-, 594-, 635-, 746-, or 749-keV γ-ray must be observed in any of the focal plane clovers in prompt coincidence with the 269-keV γ ray. A half-life of $3.39(9)$ μs was extracted using the logarithmic time-scale method [Schmidt00]. This half-life corresponds to reduced transition strengths of $1.26(4) \cdot 10^{-3}$ W.u. for the 269-keV $E2$ transition, and 21(3) W.u. for the 339-keV $E3$ transition.

4.2 Isomeric $^1/_2^+$ intruder states in astatine nuclei

Obtained level schemes for the $^1/_2^+$ structures in ^{199,201}At are presented in Fig. 4.6. Next the data analysis will be discussed one nucleus at a time.

4.2.1 ^{201}At

The searching of the isomeric $^1/_2^+$ state from the ^{201}At data was based on the seeking of the recoil-conversion electron chains (later R-e chains). The recoil must be identified as described in Fig. 3.5(b) and associated text, and the recoil implantation must be followed by a conversion electron in the same pixel of the DSSD within 130 ms from the recoil implantation. This time window corresponds to approximately three times the half-life of the isomeric $^1/_2^+$ state. The deduction of the half-life is explained at the end of this section. ^{201}At is an α-decaying nucleus, but the relatively long half-life (85.2(16) s [Kondev07]) with respect to the recoil implantation rate makes the α tagging unusable. However, this is not crucial because the 4n evaporation channel producing ^{201}At predominates.

Two interesting γ-ray transitions are observed in coincidence with the R-e chain electron. The energies of these γ rays are 190.1(1) and 269.1(1) keV. The γ-ray energy spectrum showing these transitions is presented in Fig. 4.7(a). The respective conversion electron energy spectra, where the electron is in coincidence with the 190- or the 269-keV γ-ray transition are presented in Figs. 4.7(b) and 4.7(c). The two peaks in these spectra represent the K- and $L + M + \ldots$-conversions of the 190- and 269-keV transitions. For the 269-keV transition the observed internal conversion intensity ratio $^K/_{L+M+\ldots} = 0.24(1)$ suggests a transition type of $E3$, as the corresponding theoretical ratio for an $E3$ transition is $0.225(5)$ [Kibédi08]. The corresponding measured ratio for the 190-keV transition is $3.1(2)$, and the calculated ratios are $4.27(9)$ ($M1$) and $0.45(2)$ ($E2$). Moreover, the 190-keV transition is in prompt coincidence with the 269-keV transition. Based on these arguments, a mixed $^{M1}/_{E2}$ character is suggested for the 190-keV transition. These transition type assignments suggest a spin and parity of $^1/_2^+$ for the isomeric state, and $^7/_2^-$ for the level between the isomeric state and the $^9/_2^-$ ground state.

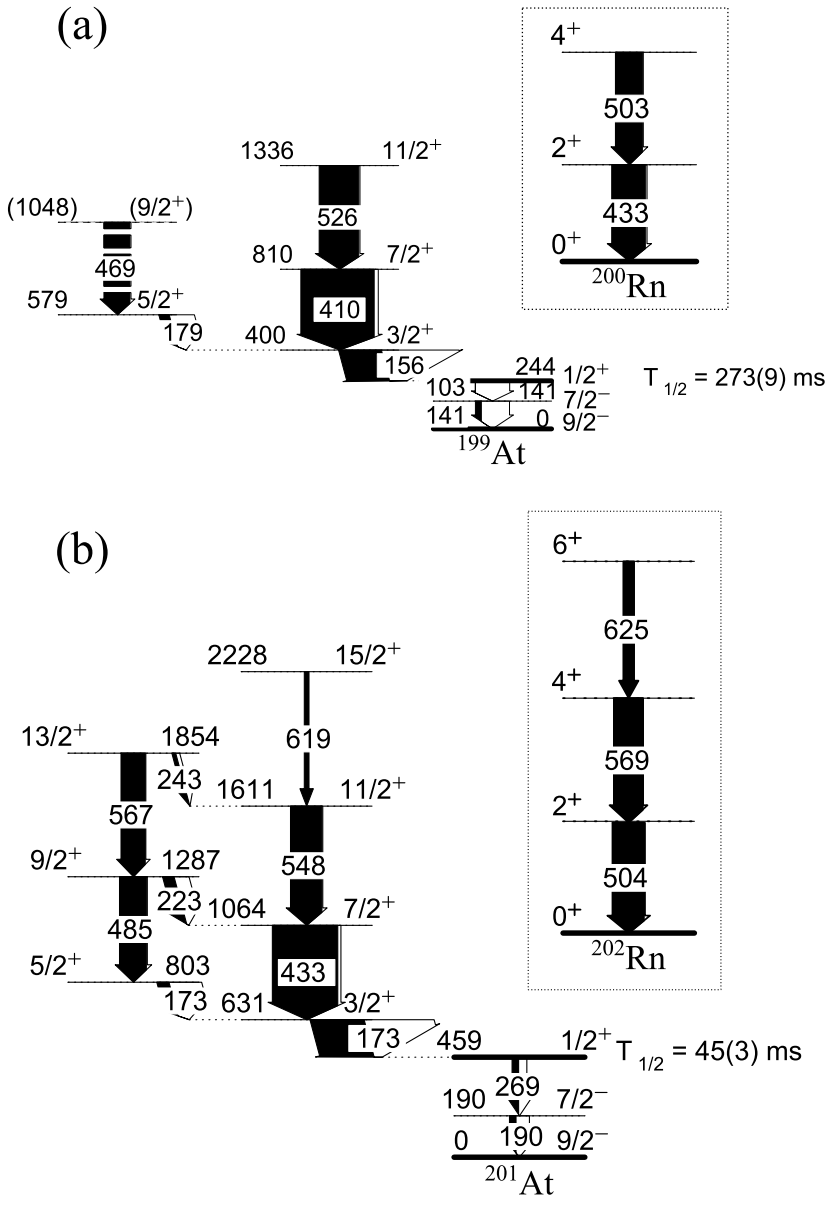

Figure 4.6: Level scheme for the excited states associated with the $1/2^+$ isomeric intruder state in (a) ^{199}At and (b) ^{201}At. For comparison (see section 5.2), partial level schemes of ^{200,202}Rn are presented. The figures are from [Auranen14].

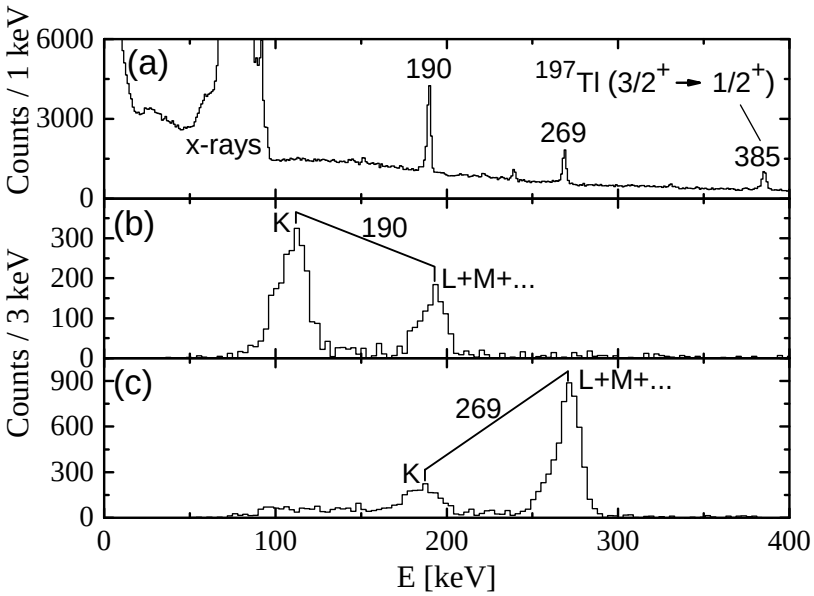

Figure 4.7: (a) R-e tagged γ-ray energy spectrum observed in the planar detector. (b) Energy spectrum of conversion electrons in coincidence with the 269-keV γ-ray transition observed in the planar detector. (c) Same as (b), but coincidence with the 190-keV γ-ray transition is demanded. The figure is from [Auranen14].

The energy spectrum of prompt γ-ray transitions associated with the $^1/_2{}^+$ isomer is presented in Fig. 4.8. For comparison, a recoil tagged spectrum is shown in panel (a). Panel (b) shows the R-e tagged energy spectrum of prompt γ-rays, where the electron is in coincidence with the 190- or 269-keV γ-transition observed in the focal plane clover array. The panel (c) shows an example of R-e tagged $\gamma\gamma$ coincidence data. Fig. 4.8(b) shows two strong γ-ray transitions, with energies of 173 keV and 433 keV. Because the 173-keV transition has a higher transition intensity, it is assumed to feed the $^1/_2{}^+$ isomer. Observed γ-ray transitions feeding the $^1/_2{}^+$ state are listed in table 4.2. The level structure feeding the $^1/_2{}^+$ state was constructed based on the $\gamma\gamma$-coincidence analysis, transition intensity balance, multipolarity information and energy sum arguments. The deduced level scheme is presented in Fig. 4.6(b).

The angular distribution parameters for the lower 173-keV transition do not

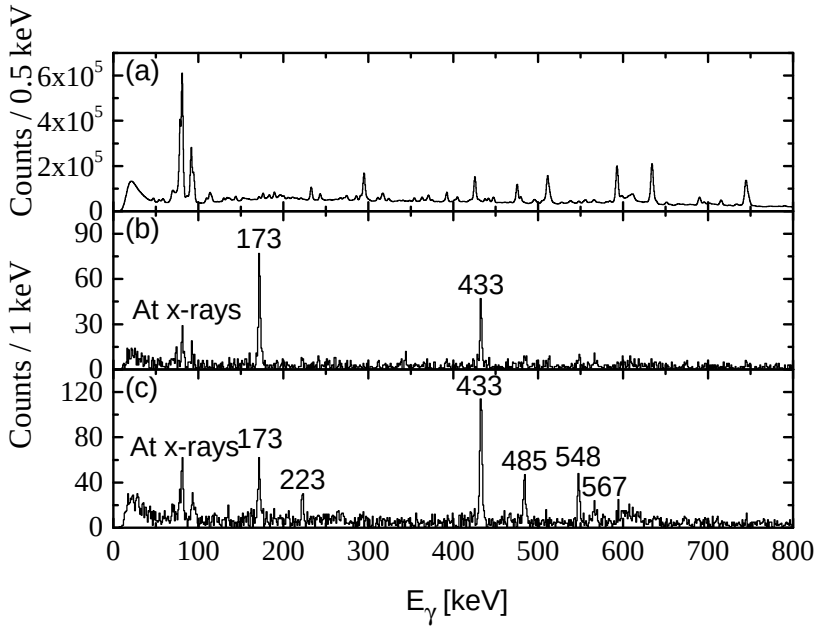

Figure 4.8: Energy spectrum of prompt γ rays observed in JUROGAM II. (a) Recoil tagged γ rays. (b) R-e tagged prompt γ-ray energy spectrum, where the recoil is in coincidence with the 190- or 269-keV γ rays observed in one of the focal plane clovers. (c) R-e tagged prompt $\gamma\gamma$-coincidence spectrum, where the gate has been set on the 173-keV transition. The figure is from [Auranen14].

point towards a pure dipole transition. This might be caused by the fact that the transition lies low in the cascade, and the spin of the decaying state is low. Therefore it is possible that the nucleus has already lost the initial alignment obtained in the fusion-evaporation reaction. Alternatively, this inconclusiveness might arise from a mixed $M1/E2$ character for the lower 173-keV transition. Assuming that there is no other decay path, in the 548-keV gated $\gamma\gamma$ spectrum the transition intensity of the lower 173-keV and 433-keV ($E2$) transitions must be equal. This suggests an $E2$ character for the lower 173-keV transition, but the x-ray intensity suggests that it cannot be a pure $E2$ type transition. Therefore a mixed $M1/E2$ character is suggested for the lower 173-keV transition.

Figure 4.9 shows the time distribution between the implantation of a recoil,

Table 4.2: Observed γ rays feeding the $^{1}/_{2}^{+}$ isomer in ^{201}At. The intensities I_γ are from R-e tagged singles γ data if not specified.

E_γ [keV]	I_γ [%]	A_2[1]	R[1]	$I_i^\pi[\hbar]$	$I_f^\pi[\hbar]$
172.6(4)	113(5)[2]		0.83(5)	$^{3}/_{2}^{+}$	$^{1}/_{2}^{+}$
172.5(4)	18(1)[2]			$^{5}/_{2}^{+}$	$^{3}/_{2}^{+}$
223.3(4)	17(1)	-0.29(7)	0.74(12)	$^{9}/_{2}^{+}$	$^{7}/_{2}^{+}$
242.8(7)	5.7(5)[3]			$^{13}/_{2}^{+}$	$^{11}/_{2}^{+}$
433.3(4)	100(4)		1.21(5)	$^{7}/_{2}^{+}$	$^{3}/_{2}^{+}$
484.5(4)	41(3)	0.70(6)	1.4(2)	$^{9}/_{2}^{+}$	$^{5}/_{2}^{+}$
548.1(4)	48(2)	0.5(2)	1.26(12)	$^{11}/_{2}^{+}$	$^{7}/_{2}^{+}$
567.3(4)	37(2)	0.5(3)	1.2(3)	$^{13}/_{2}^{+}$	$^{9}/_{2}^{+}$
618.8(6)	7(3)[3]	0.6(4)	1.1(4)	$^{15}/_{2}^{+}$	$^{11}/_{2}^{+}$

[1]See equations 3.8, 3.9. R is the weighted average of the parameters presented in Eq. 3.9

[2]Doublet, Intensity from 173-keV gated, recoil-correlated $\gamma\gamma$-data.

[3]Weak transition, intensity from 173-keV gated, recoil-correlated $\gamma\gamma$-data.

and the subsequent (conversion) electron. The 130-ms time gate is omitted in this case. From the figure one may conclude that the background originating mainly from β^+ decay and electron capture dominates the distribution. Because of this the conversion electrons were enhanced by demanding a coincidence with the 190- or 269-keV γ ray. In addition the recoil was identified by demanding a 173- or 433-keV prompt γ ray to be observed in JUROGAM II. These two requirements reduce the background notably. Fitting a two-component function [Schmidt00] to the remaining $^{1}/_{2}^{+}$ activity and the β^+/EC background yields a half-life of 45(3) ms for the isomeric $^{1}/_{2}^{+}$ state.

4.2.2 ^{199}At

The search for the $^{1}/_{2}^{+}$ isomer in ^{199}At was based on looking for recoil-conversion electron-^{199}At α decay chains (later R-e-α chains) in the same pixel of the DSSD within certain search times. The half-life of the $^{1}/_{2}^{+}$ isomer is estimated to be 310(80) ms [Jakobsson13], hence the search time between the recoil implantation and the subsequent conversion electron was set to 1 s. Moreover, the half-life of the ^{199}At ground state is 7.03(15) s [Singh07], hence

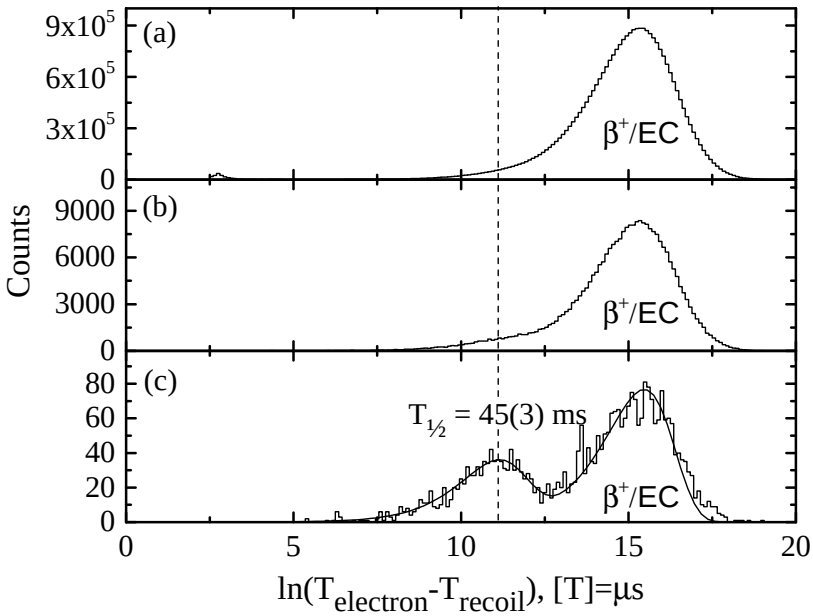

Figure 4.9: Logatithm of the time difference between the implantation of the recoil and the subsequent electron in the same pixel of the DSSD. (a) all R-e chains. (b) Electron in coincidence with the 190- or 269-keV γ ray observed at the focal plane. (c) same as (b), but in addition the recoil must be associated with the 173- or 433-keV γ ray observed in JUROGAM II. The logarithmic time-scale method yields a half-life of 45(3) ms for the isomeric $1/2^+$ state. The figure is from [Auranen14].

a search window of 21 s was allowed between the conversion electron and the subsequent ^{199}At α particle.

The $1/2^+$ state in ^{199}At is known to deexcite through a $\sim$90-keV $E3$ transition [Jakobsson13]. Fig. 4.10(a) shows the conversion electron energy spectrum, where the electron belongs to a R-e-α chain. The peak at the lower energy of 103(2)[1] keV corresponds to the $L + M + \ldots$ internal conversion decay of the $1/2^+$ isomer. The K-conversion is weak due to the low transition energy [Kibédi08]. The peak at an energy of $\sim$160 keV is the sum of $L + M + \ldots$ conversion of the 103-keV transition and the K-conversion of the subsequent

[1]Energy value obtained from the R-e-α tagged conversion electron spectrum, where the electron is in coincidence with a 141-keV γ-ray transition observed in the planar detector.

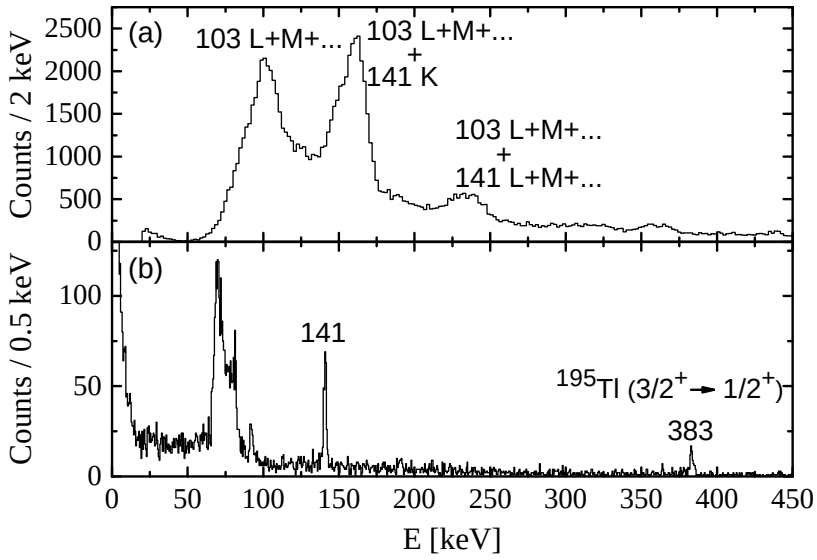

Figure 4.10: (a) Energy spectrum of conversion electrons associated with R-e-α chains. (b) R-e-α tagged energy spectrum of γ rays observed in the planar detector in coincidence with the 103-keV conversion electron. The figure is from [Auranen14].

141-keV transition. Figure 4.10(b) presents the γ rays in coincidence with the R-e-α chain electron observed in the planar detector. In this spectrum there is a transition at an energy of 141.0(1) keV. The wide peak at an energy of $\sim$ 75 keV is a result of random coincidences with β particles. This peak contains a continuum of x-rays from astatine down to platinum. The K-conversion of the 141-keV transition is rarely observed alone, because of the high $L + M + \ldots$-conversion of the 103-keV transition ($\alpha_{\mathrm{L+M+...}} = 180(5)$, [Kibédi08]). The 141-keV transition is suggested to be of $M1$ character based on the high x-ray yield. Moreover, the half-life of the $^1/_2{}^+$ state, lack of x-rays in coincidence with the 141-keV transition, and the systematics in this part of the nuclear chart indicate that the 103-keV transition type is $E3$. Based on these arguments the spin and parity of the isomeric state is suggested to be $^1/_2{}^+$, and the level between the $^9/_2{}^-$ ground state and the isomeric state is $^7/_2{}^-$. This is identical to the corresponding system in ^{201}At presented earlier.

The observed γ-ray transitions feeding the isomeric $^1/_2{}^+$ state are listed in

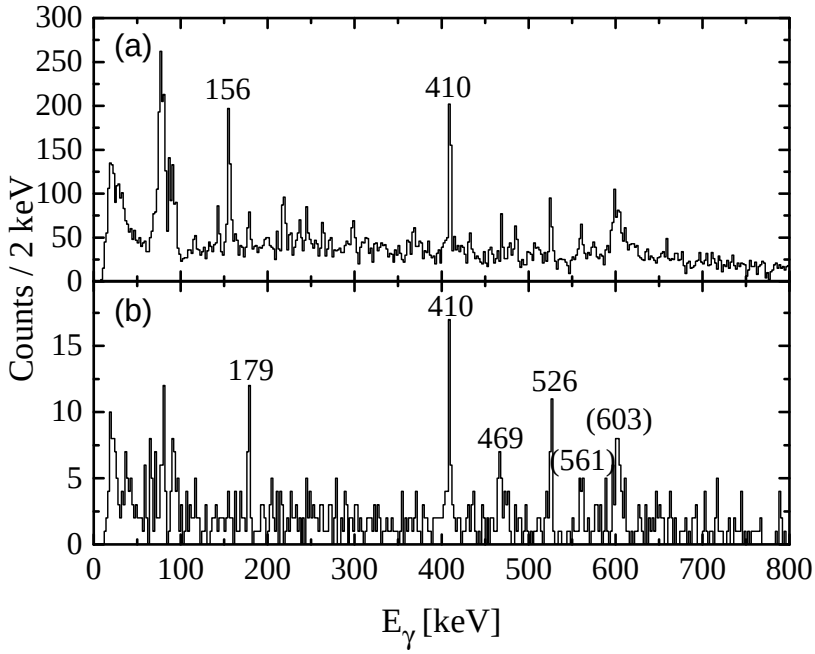

Figure 4.11: Energy spectrum of R-e-α tagged prompt γ rays observed in JUROGAM II. (a) An electron energy gate of ∼160 keV demanded. (b) γ rays in coincidence with the 156-keV prompt γ ray. Transitions in parenthesis belong to ^{199}At Band 1 [Jakobsson10] or ^{199}Po [Singh07]. The figure is from [Auranen14].

table 4.3. The 156-keV transition is suggested to be of mixed $M1/E2$ character based on the same reasons as listed in the case of the lower 173-keV transition in ^{201}At. Fig. 4.11(a) shows the energy spectrum of prompt R-e-α tagged γ rays observed in JUROGAM II. An electron energy of ∼160 keV has been demanded. The spectrum is dominated by two transitions, the energies of which are 156 and 410 keV. The 156-keV transition has a higher transition intensity, hence it is assumed to feed the $1/2^+$ state. In Fig. 4.11(b) an example of R-e-α tagged $\gamma\gamma$ analysis is shown. The level scheme above the $1/2^+$ state was constructed based on the $\gamma\gamma$ coincidence information, angular distribution information, intensity balance and energy sum arguments. The deduced level scheme is presented in Fig. 4.6(a). The spin and parity of the level deexcited by the 469-keV transition is left tentative, regardless of the fact that the transition type is known. The systematics in this part of the nuclide chart suggests

Table 4.3: Observed γ rays feeding the $^{1}/_{2}^{+}$ isomer in ^{199}At. If not specified, values are obtained from R-e-α tagged singles data.

E_γ [keV]	I_γ [%]	A_2[1]	R[1]	$I_i^\pi[\hbar]$	$I_f^\pi[\hbar]$
156.1(4)	100(6)		0.8(2)[2]	$^{3}/_{2}^{+}$	$^{1}/_{2}^{+}$
179.0(5)	17(4)		0.82(14)	$^{5}/_{2}^{+}$	$^{3}/_{2}^{+}$
410.2(4)	124(6)	0.05(3)	1.24(8)	$^{7}/_{2}^{+}$	$^{3}/_{2}^{+}$
469.4(4)	44(3)		1.8(7)[3]		
526.0(4)	67(4)		1.31(13)	$^{11}/_{2}^{+}$	$^{7}/_{2}^{+}$

[1] See equations 3.8, 3.9.

[2] R value obtained from $\gamma\gamma$-data using sum gate over all other transitions.

[3] R value obtained from 156 keV gated $\gamma\gamma$-data.

that the 469-keV transition should feed the level deexcited by the 179-keV transition. This situation is analogous to the case of the higher 173- and the 485-keV transition in ^{201}At. However, due to low statistics in $\gamma\gamma$ data this coincidence was not confirmed in ^{199}At.

The half-life of the $^{1}/_{2}^{+}$ isomeric state was deduced in similar manner to the case of ^{201}At. This is shown in Fig. 4.12. The logarithmic time-scale method produces a half-life of 273(9) ms for the isomeric $^{1}/_{2}^{+}$ state.

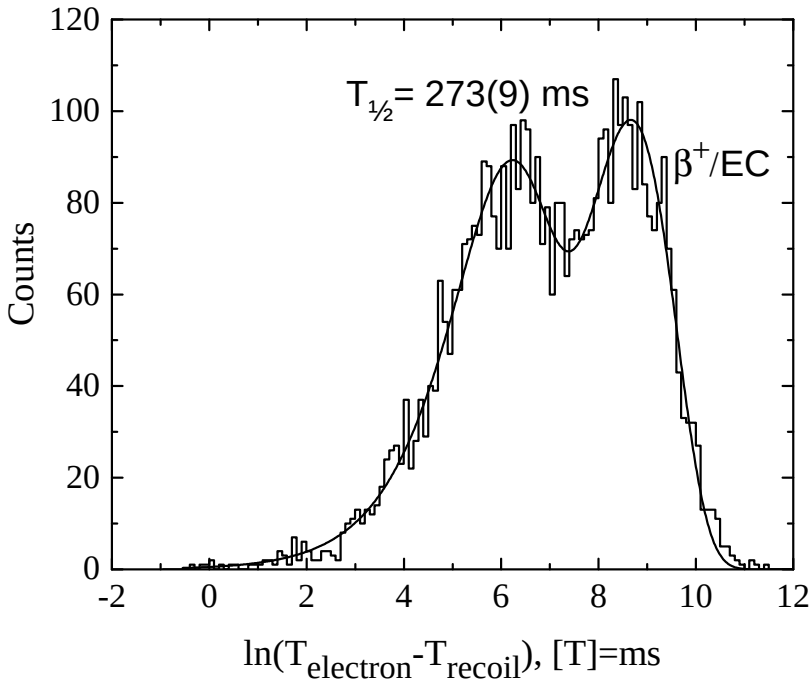

Figure 4.12: Logarithm of the time difference between the implantation of the R-e-α tagged recoil and the subsequent electron in the same pixel of the DSSD. In addition to the R-e-α chain the 156- or 410-keV γ-ray transition must be observed in JUROGAM II. In this analysis the 1 s recoil-electron time gate was neglected. The logarithmic time-scale method yields a half-life of 273(9) ms for the isomeric $^1/_2{}^+$ state. The figure is from [Auranen14].

4.3 Shears band in ^{201}At

Figure 4.13 presents a recoil tagged, double gated energy spectrum of prompt γ rays. The other gate is a sum of gates 145, 198, 244, 272, 287, 317 or 335 keV, and the other gate is a sum of gates 427 or 746 keV. In the spectrum the transitions labeled with energy are suggested to have $M1$ character. This is supported by the dipole-like angular distribution of γ rays, and high x-ray intensity in coincidence with these transitions. These transitions are listed in Table 4.4. There could be weak $E2$ cross-over transitions, but these were not

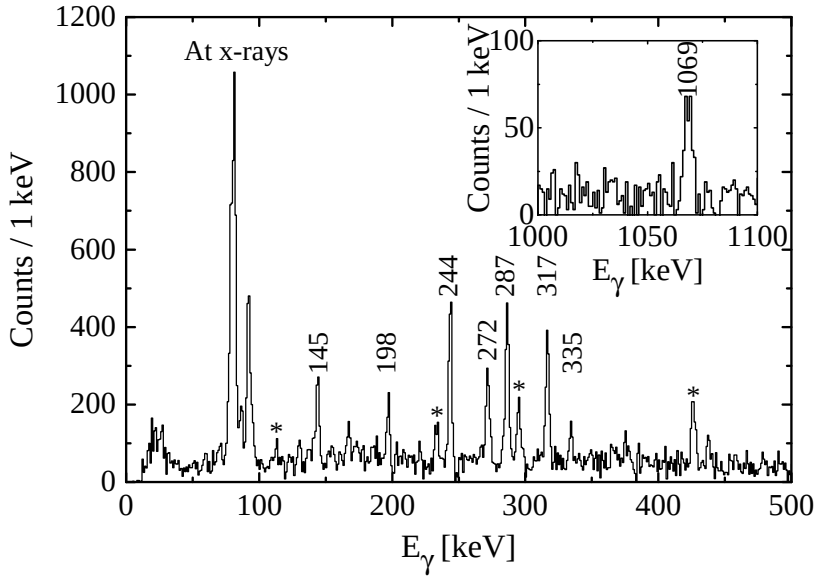

Figure 4.13: Recoil-gated prompt γ rays in coincidence with one of the low-energy transitions listed in Table 4.4 and either the 427- or the 746-keV γ ray. Transitions with an energy label are suggested to form a shears band. Transitions marked with an asterisk belong to the positive parity cascade. The inset shows the high-energy part of the spectrum. The figure is from [Auranen14].

observed. The lower limits for the $B(M1)/B(E2)$ ratios were extracted[2] by integrating the smallest observable peak near the energy of the unobserved $E2$ transition.

Based on the $\gamma\gamma$ and $\gamma\gamma\gamma$ coincidences, these $M1$ transitions form a cascade, which is suggested to form a shears band (See section 5.3). In coincidence with this shears band there is a 1069-keV dipole transition. This transition and the transitions in the proposed shears band are in coincidence with the 296- and 427-keV transitions, but not with the 83-keV transition. Based on this coincidence analysis, the shears band is suggested to depopulate through the 1069-keV transition to the $^{21}/_{2}^{+}$ state. The magnetic or electric character of the 1069-keV dipole transition cannot be established from the information produced in this experiment. Moreover, the transition intensity of the 145-

[2]See equation 2.15

Table 4.4: Observed γ-ray transitions associated with the shears band in ^{201}At. Intensities I_γ are normalized such that $I_\gamma(635\text{ keV}) = 100$. Intensities and energies are deduced from the sum of gates (746-, 427-keV transitions) $\gamma\gamma$ data.

E_γ [keV]	I_γ	A_2[1]	$I_i^\pi[\hbar]$	$I_f^\pi[\hbar]$	$B(M1)/B(E2)$ $[\mu_N^2/e^2b^2]$
145.0(4)	3.7(3)	-0.5(2)	$(^{25}/_2^-)$	$(^{23}/_2^-)$	-
197.9(4)	1.6(2)	-0.80(12)	$(^{35}/_2^-)$	$(^{33}/_2^-)$	>8
244.4(4)	8.3(5)	-0.59(9)	$(^{27}/_2^-)$	$(^{25}/_2^-)$	>30
272.3(4)	3.5(3)	-0.45(11)	$(^{33}/_2^-)$	$(^{31}/_2^-)$	>35
286.9(4)	6.6(4)	-0.47(3)	$(^{29}/_2^-)$	$(^{27}/_2^-)$	>25
317.3(4)	6.7(4)	-0.81(9)	$(^{31}/_2^-)$	$(^{29}/_2^-)$	>30
335.0(4)	1.5(2)	-0.66(4)	$(^{37}/_2^-)$	$(^{35}/_2^-)$	>2
1068.9(4)	4.5(3)	-0.47(5)	$(^{23}/_2^-)$	$^{21}/_2^+$	

[1]See equation 3.8.

keV transition is much higher than the transition intensity of the 1069-keV transition, hence there must be at least one additional, unobserved decay path. The parity assignment of the shears cascade is discussed in section 5.3.

4.4 Other observed transitions and levels in ^{201}At

There is a large number of γ-ray transitions in addition to transitions in the shears band and the transitions below the isomeric $^{29}/_2^+$ state. These transitions can be divided into three groups. The transitions feeding the $^{21}/_2^+$ and $^{29}/_2^+$ states form groups 1 and 2, respectively. The third group is formed by the transitions in the negative parity band. Most of the transitions belonging to groups 1 and 2 are observable in Figs. 4.14(a) and 4.14(b), respectively. Panel (a) shows the energy spectrum of γ rays in coincidence with the 716-keV transition. The transitions connected with a dashed line form group 1 together with the 716-keV transition. Panel (b) shows the γ-ray singles spectrum, where the recoil has been isomer tagged with a 269-, 427-, 635-, 746-, or 749-keV delayed γ-ray transition observed in the GREAT clover array within 14 μs from the recoil implantation. The transitions with energy labels are those that

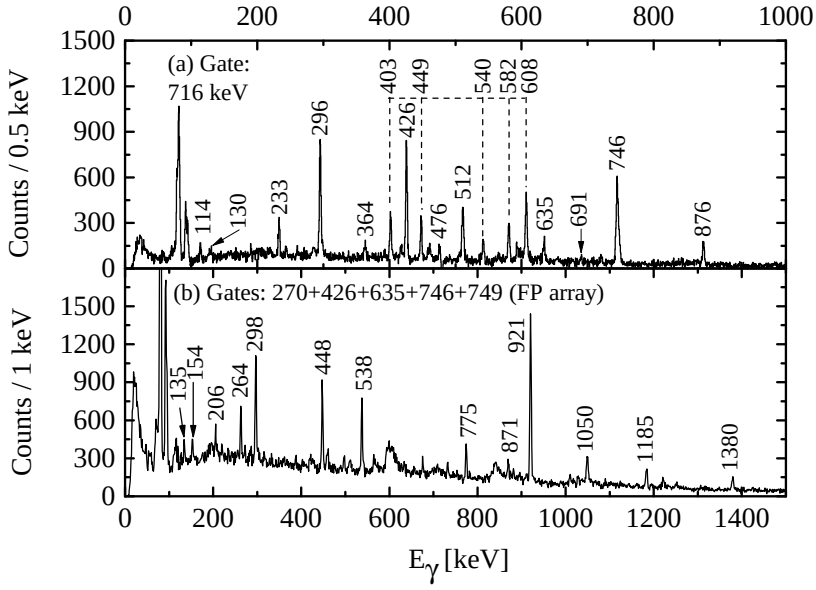

Figure 4.14: Prompt γ-ray transitions observed in the JUROGAM II array: (a) γ-ray transitions in coincidence with the 716-keV transition. Transitions connected by a dashed line form the group 1 together with the 716-keV transition. (b) Singles γ-ray energy spectrum, where a delayed coincidence is demanded with any of the most intense γ-ray transitions (observed in any of the focal plane clovers) depopulating the $^{29}/_{2}^{+}$ isomeric state. Note the different energy scales in (a) and (b) panels.

feed the isomeric $^{29}/_{2}^{+}$ state. The transitions belonging to groups 1-3 are listed in table 4.5 and the corresponding level schemes are presented in Fig. 4.4. The level scheme was built based on the $\gamma\gamma(\gamma)$ coincidence analysis, transition intensity balance and energy sum arguments.

4.5 Other observed transitions and levels in ^{199}At.

The ^{199}At nucleus has been studied previously at JYFL, and the level scheme is relatively well known [Jakobsson10]. In the previous experiment in-beam spectroscopy was performed using the $p2n$ fusion-evaporation channel with a cross section of $10 - 15$ μb. The $6n$ reaction channel used in this study has

Table 4.5: Additional observed γ-ray transitions in ^{201}At. Information for group 1 transitions is obtained from the sum-gated (296-, 427-keV transitions) $\gamma\gamma$ data. Information for group 2 is obtained from the 269-, 427-, 635-, 749- or 749-keV delayed γ-ray tagged singles spectrum. Group 3 information is obtained from recoil-gated singles data. I_γ is normalized such that $I_\gamma(635\ \text{keV}) = 100$.

Group	E_γ [keV]	I_γ	A_2[1]	$I_i^\pi[\hbar]$	$I_f^\pi[\hbar]$
1	402.6(4)	2.6(3)	-0.7(2)		
1	448.5(4)	2.8(2)	-0.4(2)		
1	540.5(5)	3.1(3)			
1	581.6(4)	2.1(2)	-0.44(7)		
1	607.8(4)	8.4(8)	0.35(8)	$(^{29}/_2{}^+)$	$(^{25}/_2{}^+)$
1	716.3(4)	11.9(7)	0.46(4)	$(^{25}/_2{}^+)$	$^{21}/_2{}^+$
2	135.0(4)	0.50(4)			
2	153.6(4)	0.47(4)			
2	206.2(4)	0.31(5)			
2	263.6(4)	1.2(2)	-0.26(9)		
2	297.5(4)[2]	3.0(2)			
2	448.4(4)	2.9(2)	-0.3(2)		
2	538.2(4)	2.9(2)			
2	774.9(4)[2]	1.7(2)	0.29(4)		
2	870.5(4)	0.93(8)			
2	921.1(4)	10.1(6)	0.20(3)	$(^{33}/_2{}^+)$	$^{29}/_2{}^+$
2	1049.9(4)	2.2(2)	-0.7(3)		
2	1184.5(4)	1.7(2)	0.40(8)		
2	1379.9(5)	1.4(2)			
3	371.7(4)	10.9(4)	0.16(6)	$^{25}/_2{}^-$	$^{21}/_2{}^-$
3	442.6(4)	6.0(2)	0.35(8)	$^{21}/_2{}^-$	$^{21}/_2{}^-$
3	917.8(4)	7.0(4)	0.37(6)	$^{21}/_2{}^-$	$^{17}/_2{}^-$

[1]See equation 3.8.

[2]Transition is not placed in the level scheme, as it is not in coincidence with other transitions.

a cross section of ~ 160 μb, which together with a slightly longer beam time leads to significantly higher statistics compared to the previous experiment. This is demonstrated in Fig. 4.15, where the γ-ray energy spectrum of prompt transitions tagged with the α decay of ^{199}At is shown. With the higher statistics obtained in this study it was possible to confirm the existing level scheme. However, it was not possible to extend it. This might be caused by a few reasons. Firstly, the decay path of γ rays from more highly excited states can be fragmented, see Fig. 3.2(c). Observation of such γ rays depopulating levels away from the yrast line is very demanding and requires a huge amount of statistics. Secondly, the existence of an isomeric state with a half-life of $\sim 50 - 500$ ns cannot be excluded. The existence of such an isomeric state would lead to internal transition in flight inside the RITU separator, and would have been unobservable with the present experimental setup. Thirdly, fission may cut the population of high-spin states. Therefore the number of

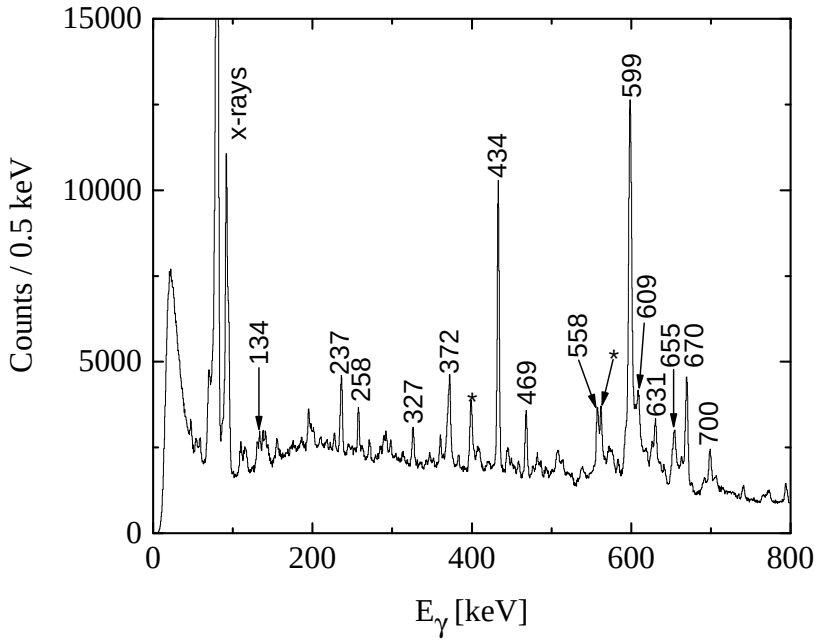

Figure 4.15: Energy spectrum of prompt γ ray singles tagged with the ^{199}At α decay. Transitions observed previously [Jakobsson10] are labeled with energy. Transitions marked with an asterisk most likely belong to ^{199}Po [Singh07].

^{199}At recoils with high excitation energy after the fusion evaporation would be smaller than the number of ^{199}At recoils with smaller excitation energy. This reduces the intensity of high-spin γ rays, and makes them more difficult to observe.

Chapter 5

Discussion

5.1 Isomeric $^{29}/_{2}^{+}$ state in ^{201}At and the subsequent levels

Figure 5.1 shows a comparison between negative parity states in odd-mass astatine and the yrast states in their polonium isotones. From the figure it is easy to notice that in astatine nuclei levels up to $^{21}/_{2}^{-}$ state follow the energies of the yrast states in their even-even polonium isotones. This similarity supports the earlier suggestion that in ^{201}At these levels originate from the weak coupling of the $h_{9/2}$ proton to the polonium core [Dybdal83]. This interpretation is also suggested for ^{199}At [Jakobsson10], ^{203}At [Dybdal83], and ^{205}At [Sjoreen82]. The deviation of the level spacing in ^{197}At is suggested to originate from the strengthening of the proton coupling to the core [Jakobsson10]. In the lighter astatine isotopes the intruding $^{1}/_{2}^{+}$ state originating from the $\pi(s_{1/2})^{-1}$ configuration becomes the ground state, hence the schemes of observed excited states changes [Kettunen03a, Kettunen03b]. For the nearby francium nuclei it has also been suggested that the negative parity states originate from the coupling of the $h_{9/2}$ proton to the radon core, see [Jakobsson13] for ^{203}Fr (isotone of ^{201}At) and [Jakobsson12] for ^{205}Fr (^{201}At+α particle).

Table 5.1 lists a few selected excited states in ^{200}Po, the isotonic partner of

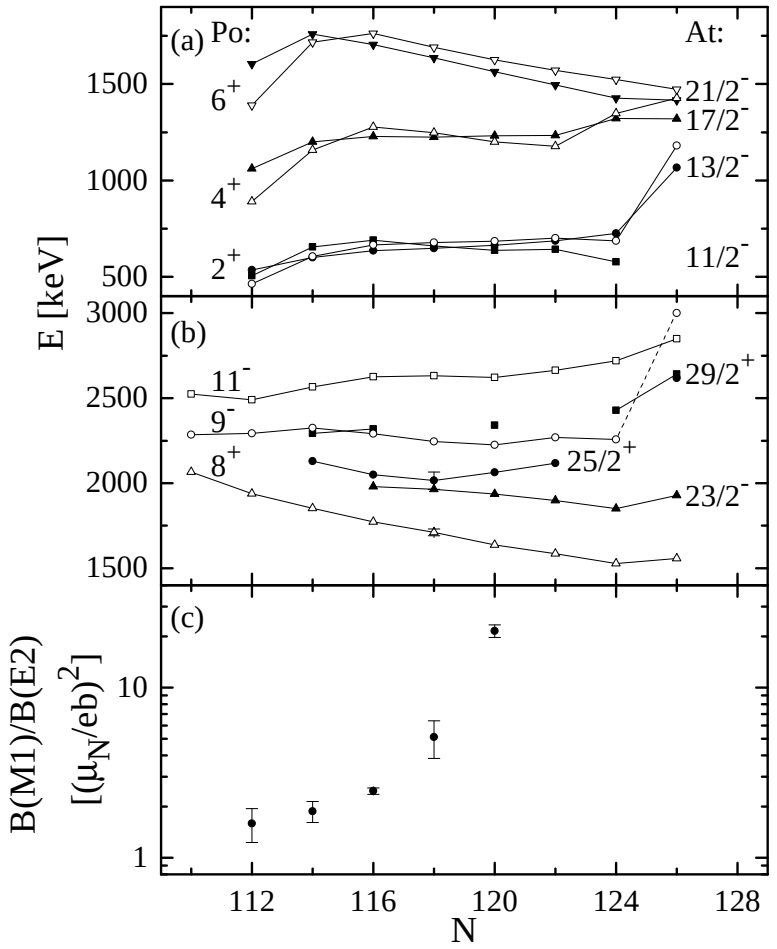

Figure 5.1: Energy systematics of the selected astatine (solid symbols) and polonium (open symbols) states: (a) Negative parity levels in astatine are compared to the yrast states of their polonium isotones. (b) Level energies of the $^{29}/_{2}^{+}$, $^{25}/_{2}^{+}$ and $^{23}/_{2}^{-}$ states in astatine are compared to the 11^{-}, 9^{-} and 8^{+} sates in the corresponding polonium isotones. The data points with error bars are floating in the level scheme. Panel (c) shows the measured $B(M1)/B(E2)$ ratios for the decays of the lowest $^{17}/_{2}^{+}$ states in the odd mass astatine isotopes. Data for all panels are taken from [Helariutta99, Dybdal83, Jakobsson10, Davie84, Sjoreen76, Bergström70, Sjoreen81, Bernstein95, Mann88, Andgren08, Poletti97, Beuscher76, Baxter90] and the present experiment. The neutron number of ^{201}At is 116. The figure is from [Auranen15].

Table 5.1: Selected excited states and their suggested single particle configurations observed in ^{200}Po [Weckström85, Maj90].

E [keV]	I^{π}	Configuration
2716	8_3^+	$\pi(i_{13/2}^{-2})$
2596	11^-	$\pi(h_{9/2}i_{13/2})$
2261	9^-	$\nu(f_{5/2}^{-1}i_{13/2}^{-1})$
2237	8^-	
∼2200	8_2^+	$\pi(h_{9/2}f_{7/2})$
2136	7^-	$\nu(f_{5/2}^{-1}i_{13/2}^{-1})$
1811	5^-	$\nu(f_{5/2}^{-1}i_{13/2}^{-1})$
1774	8_1^+	$\pi(h_{9/2}^2)$

^{201}At. In ^{200}Po the isomeric 11^- state decays to 9^- and 8_1^+ states through $E2$ and $E3$ type transitions, respectively. In Fig. 5.1(b) the level energies of the polonium states are compared to the energies of $^{29}/_{2}^{+}$, $^{25}/_{2}^{+}$ and $^{23}/_{2}^{-}$ states in astatine nuclei. The level energy of the isomeric $^{29}/_{2}^{+}$ state in astatine appears to follow the level energy of the isomeric 11^- state in polonium. Also the energies of $^{25}/_{2}^{+}$ and $^{23}/_{2}^{-}$ states seem to follow the energies of the 9^- and 8_1^+ states, respectively. Based on these similarities, it is suggested that the observed isomeric and the subsequent states in astatine originate from the coupling of the odd proton to the corresponding state of the polonium core. These configurations are summarized in Table 5.2, and they are identical to the interpretations proposed earlier for corresponding states in neighboring astatine nuclei [Dybdal83, Jakobsson10, Davie84].

The observed isomeric $^{29}/_{2}^{+}$ state decays through 269-keV $E2$ and 339-keV $E3$ transitions. The reduced transition strengths for these transitions are $1.26(4) \cdot 10^{-3}$ W.u. and 21(3) W.u., respectively. The hindrance of the $E2$ transition is understandable as it requires significant changes of $\pi(h_{9/2}^2 i_{13/2}) \rightarrow \pi(h_{9/2})\nu(f_{5/2}^{-1}i_{13/2}^{-1})$ to the single particle configuration. The changes in the $E3$ transition are much simpler, $\pi(h_{9/2}^2 i_{13/2}) \rightarrow \pi(h_{9/2}^2 f_{7/2})$, and it involves octupole correlations hence it is enhanced [Bergström85]. The measured reduced transition strengths are comparable with the corresponding values of $\sim 10^{-2}$ and ~ 12 W.u. for the $E2$ ($11^- \rightarrow 9^-$) and $E3$ ($11^- \rightarrow 8_1^+$) transitions in ^{200}Po [Weckström85], respectively. This comparison is also presented in

Table 5.2: Suggested configurations for some of the observed excited states in ^{201}At.

E [keV]	I [$\hbar$]	Configuration
635	$13/2^-$	$\pi(h_{9/2}) \otimes \vert^{200}\text{Po}; 2^+\rangle$
691	$11/2^-$	$\pi(h_{9/2}) \otimes \vert^{200}\text{Po}; 2^+\rangle$
749	$13/2^+$	$\pi(i_{13/2}) \otimes \pi(h_{9/2})^2_{0+}$
1229	$17/2^-$	$\pi(h_{9/2}) \otimes \vert^{200}\text{Po}; 4^+\rangle$
1495	$17/2^+$	$\pi(i_{13/2}) \otimes \pi(h_{9/2})^2_{2+}$
1705	$21/2^-$	$\pi(h_{9/2}) \otimes \vert^{200}\text{Po}; 6^+\rangle$
1625	$17/2^+$	$\pi(h_{9/2}) \otimes \vert^{200}\text{Po}; 5^-\rangle$
1980	$23/2^-$	$\pi(f_{7/2}) \otimes \vert^{200}\text{Po}; 8^+_1\rangle$
1921	$21/2^+$	$\pi(h_{9/2}) \otimes \vert^{200}\text{Po}; 7^-\rangle$
2005	$23/2^+$	$\pi(h_{9/2}) \otimes \vert^{200}\text{Po}; 8^-\rangle$
2050	$25/2^+$	$\pi(h_{9/2}) \otimes \vert^{200}\text{Po}; 9^-\rangle$
2148	$21/2^-$	$\pi(f_{7/2}) \otimes \vert^{200}\text{Po}; 8^+_2\rangle$
2319	$29/2^+$	$\pi(h_{9/2}) \otimes \vert^{200}\text{Po}; 11^-\rangle$
2519	$25/2^-$	$\pi(h_{9/2}) \otimes \vert^{200}\text{Po}; 8^+_3\rangle$

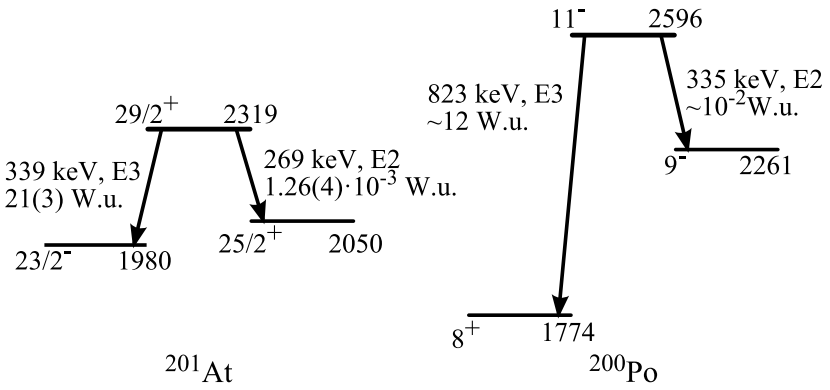

Figure 5.2: Depopulation of the $^{29}/_2{}^+$ and 11^- isomeric states in ^{201}At and ^{200}Po, respectively.

Fig. 5.2. The $^{29}/_{2}^{+}$ state has also been observed in ^{199}At [Jakobsson10], ^{205}At [Davie84], ^{209}At [Sjoreen76], and ^{211}At [Bergström70]. In ^{199}At only the $E2$ transition has been observed to depopulate the $^{29}/_{2}^{+}$ state with a reduced transition strength of 0.044 W.u. In ^{205}At both transitions have been observed with a strengths of $1.8(5) \cdot 10^{-4}$ W.u. ($E2$) and 19(1) W.u. ($E3$). In ^{209}At and ^{211}At only the $E3$ transition has been observed with reduced transition strengths of 24(2) W.u. and 16 W.u., respectively [Davie84]. Consequently, the observed reduced transition strength values in ^{201}At are comparable with the respective values of neighboring nuclei.

From Fig. 5.1(b) one can also notice that the transition energy of the $E3$ transition decreases more rapidly than the transition energy of the $E2$ transition as the neutron number decreases. As a result of this, the depopulation of the $^{29}/_{2}^{+}$ state favors the $E2$ transition in lighter, and $E3$ transition in heavier astatine isotopes. Also the reduced transition strength increases as the neutron number decreases for the $E2$ transition, making it dominate over the $E3$ transition.

The $^{25}/_{2}^{+}$ states have been observed previously in ^{207,205,203}At, and those are reported to have mean lifetimes of 156(3), 98(2), and 17(2) ns, respectively [Sjoreen81, Davie84, Dybdal83]. If the mean lifetime of the $^{25}/_{2}^{+}$ state develops as might be expected, it should be much shorter than $\sim$20 ns in ^{201}At. The experimental setup (100 MHz clock, 10 ns time resolution) used in this study is not sensitive for lifetimes this short. An attempt was made to extract the lifetime of the $^{13}/_{2}^{+}$ state, previously reported to be 23(2) ns [Dybdal83]. As a result a time distribution yielding a lifetime of $\sim$20 ns was achieved. A similar analysis for the lifetime of the $^{25}/_{2}^{+}$ state resulted a prompt-like time distribution. Hence the mean lifetime of the $^{25}/_{2}^{+}$ state is shorter than $\sim$20 ns.

The $^{13}/_{2}^{+}$ state in odd-mass astatine isotopes $^{197-205}$At is suggested to originate from the $\pi(i_{13/2})$ configuration [Dybdal83, Jakobsson10, Davie84]. In astatine nuclei ^{197,199}At the $^{13}/_{2}^{+}$ state is fed by a strongly coupled rotational band, and the $^{13}/_{2}^{+}$ state is suggested to be oblate deformed [Jakobsson10, Andgren08]. In ^{201}At only levels up to the lowest $^{17}/_{2}^{+}$ state show rotational-like pattern. In any levels higher than this, the rotational-like behavior disappears. Figure 5.1(c) shows the $B(M1)/B(E2)$ ratios for the decay of the lowest $^{17}/_{2}^{+}$ state in astatine nuclei. In isotopes lighter than ^{201}At the ratio

is close to unity and quite constant. However, starting from ^{201}At the ratio grows rapidly as the neutron number increases. The disappearing of the rotational structure and the mentioned behavior of the $B(M1)/B(E2)$ ratio might indicate a decrease of deformation in heavier isotopes. Based on this, the $^{13}/_{2}^{+}$ state is suggested to be weakly oblate in ^{201}At.

The lowest 2^+ state in ^{198}Pb lies at the energy of 1064 keV [Honkanen86]. This is comparable to the transition energy of the transitions feeding the $^{29}/_{2}^{+}$ isomer. This might suggest that the states feeding the $^{29}/_{2}^{+}$ state have a $\pi(h^2_{9/2}i_{13/2}) \otimes |^{198}\mathrm{Pb};2^+_1\rangle$ -like single particle configuration.

5.2 Isomeric $^{1}/_{2}^{+}$ intruder states in astatine nuclei

The observations related to the isomeric intruder $^{1}/_{2}^{+}$ state in ^{199}At agree well with previous results [Jakobsson13]. The extracted half-life of 273(9) ms agrees well with the earlier result of 310(80) ms. Consequently the extracted reduced transition strength of 0.09(2) W.u. for the $E3$ transition is also consistent. A branch of $\sim$1 % was predicted earlier [Jakobsson13] for the α decay of the $^{1}/_{2}^{+}$ state by assuming an unhindered α decay. However, in this study we did not observe such an α decay. The current experiment is the first one to report the $^{1}/_{2}^{+}$ state in ^{201}At. The results agree well with the systematics, and the measured reduced transition strength of 0.050(3) W.u. is comparable with the values in neighboring astatine nuclei (0.09 W.u. ^{199}At, 0.07 W.u. ^{195}At [Nyman13]).

Figure 5.3 presents the systematics of the $^{1}/_{2}^{+}$ state level energies in odd-Z nuclei close to $Z = 82$ magic shell gap. From this figure it is easy to see that level energy of the $^{1}/_{2}^{+}$ state decreases as the neutron number decreases. This is characteristic for the intruder states in this region of the nuclear chart. The $^{1}/_{2}^{+}$ states presented in Fig. 5.3 are known to originate from the $\pi(s_{1/2})^{-1}$ configuration (see references listed in Fig. 5.3). The level energies obtained in this study for ^{199,201}At are consistent when compared to neighboring nuclei. Based on this similarity we propose that the $^{1}/_{2}^{+}$ states in ^{199,201}At also originates from the $\pi(s_{1/2})^{-1}$ configuration. Figure 5.3 shows also the level energies of the intruder $^{9}/_{2}^{-}$ states in thallium nuclei. The excitation mechanism in these

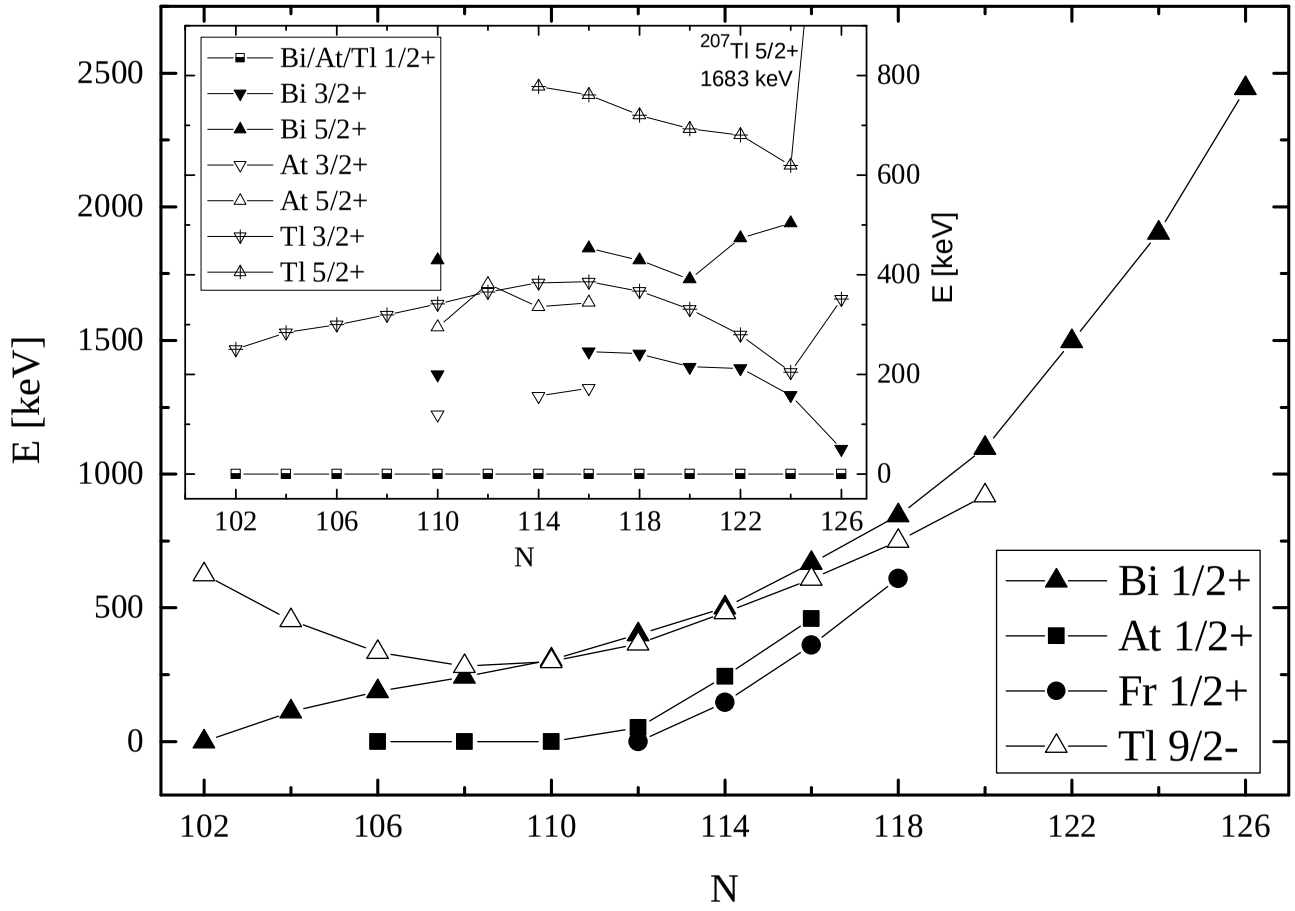

Figure 5.3: Systematics of the $1/2^+$ ($\pi(s_{1/2})^{-1}$) isomer level energies in nuclei close to lead. For a comparison the level energies of $9/2^-$ ($\pi(h_{9/2})$) states in Tl nuclei are also shown. The inset shows the level energies of states feeding the $1/2^+$ states with respect to the level energy of the $1/2^+$ state. Neutron numbers of nuclei studied in this work are 114 and 116. Data for Bi nuclei are taken from [Andreyev04, Kettunen03a, Singh07, Heyde83, Coenen85, Nieminen04], for At nuclei this work and [Kettunen03b, Kettunen03a, Nyman13, Andgren08], for Fr [Jakobsson13, Uusitalo05, Jakobsson12], and for Tl [Heyde83, Coenen85, Kratschmer73, Kondev11, Lane95, Batchelder99]. The figure is from [Auranen14].

states is the same as for $^{1}/_{2}^{+}$ states, leading to a $\pi(h_{9/2})$ configuration. The $^{9}/_{2}^{-}$ state seems to follow the pattern of $^{1}/_{2}^{+}$ states in bismuth nuclei when $N \geq 108$. However, in lighter thallium nuclei the similarity vanishes.

In both nuclei a $^{7}/_{2}^{-}$ state has been observed at a relatively low excitation energy between the $^{9}/_{2}^{-}$ ground state and the $^{1}/_{2}^{+}$ isomeric state. Routhian surface calculations presented by Andgren *et al.* [Andgren08] show a strict change in the ground-state quadrupole deformation between the astatine isotopes ^{195}At and ^{197}At. In ^{195}At and lighter nuclei the ground state is oblate, whereas in ^{197}At and heavier isotopes it is nearly spherical. In lighter isotopes the $^{7}/_{2}^{-}$ state is suggested as originating from a proton occupying the Nilsson orbital $^{7}/_{2}^{-}[514]$ [Kettunen03a, Kettunen03b]. However, in heavier astatine isotopes it is more likely that the $^{7}/_{2}^{-}$ state originates from the spherical $\pi(f_{7/2})$ configuration, as it is suggested to do in ^{203,205}Fr [Jakobsson12, Jakobsson13]. In the case of the alternative $\pi(h_{9/2}) \otimes 2^{+}$ configuration, the $^{7}/_{2}^{-}$ state should lie closer to the $^{13}/_{2}^{-}$ state that is known to lie at excitation energies of 600 keV and 635 keV in ^{199,201}At, respectively [Jakobsson10, Dybdal83].

The inset in Fig. 5.3 shows the energy systematics of the $^{3}/_{2}^{+}$ and $^{5}/_{2}^{+}$ states with respect to the $^{1}/_{2}^{+}$ state in bismuth, astatine and thallium nuclei. These states have been suggested [Heyde83] to originate from $\pi(d_{3/2})^{-1}$ and $\pi(d_{5/2})^{-1}$ configurations, respectively. The observed $^{3}/_{2}^{+}$ and $^{5}/_{2}^{+}$ states in ^{199,201}At seems to follow the pattern set by the corresponding states in bismuth and thallium nuclei. Therefore the $^{3}/_{2}^{+}$ and $^{5}/_{2}^{+}$ states are suggested to originate from the $\pi(d_{3/2})^{-1}$ and $\pi(d_{5/2})^{-1}$ configurations, respectively.

The transition energies of the mixed $M1/E2$ transitions feeding the $^{1}/_{2}^{+}$ state are too small to form a rotational cascade with the transitions above them. Moreover, in both nuclei the levels on top of the $^{5}/_{2}^{+}$ state feed the levels on top of the $^{3}/_{2}^{+}$ state through low-energy $M1$ transitions, but not vice versa. These two arguments exclude the possibility of the two cascades being signature partners from the same rotational structure. The insets in Fig. 4.6(a) and 4.6(b) show a few lowest excited states in the radon isotones of ^{199,201}At. These states are suggested to originate from the coupling of harmonic vibration to single particle structures [Dobson02]. Transition energies in the radon level schemes shown are very similar when compared to the transitions feeding the $^{3}/_{2}^{+}$ and $^{5}/_{2}^{+}$ states in ^{199,201}At. Based on this similarity we propose that the

$^{3}/_{2}^{+}$ and $^{5}/_{2}^{+}$ states are still nearly spherical, and the $^{7}/_{2}^{+}$, $^{11}/_{2}^{+}$, $^{15}/_{2}^{+}$ [$^{9}/_{2}^{+}$, $^{13}/_{2}^{+}$] states originate from the coupling of $\pi(d_{3/2})^{-1}$ [$\pi(d_{5/2})^{-1}$] to the 2^{+}, 4^{+} or 6^{+} states of the radon core.

The comparison presented above is reasonable, since the $^{3}/_{2}^{+}$ and $^{5}/_{2}^{+}$ states can be described as a creation of a proton hole in the radon core. Similarly the low-lying excited states in odd-Z nuclei above shell closures are often described as a coupling of the odd proton to the lighter even-Z isotone core (see, for example [Jakobsson10, Jakobsson12, Jakobsson13]). It is worth noting that the radon isotones are nearly spherical in their ground states [Dobson02].

It is also worth noting that in both nuclei there is a possibility to bypass the isomeric state with a high-energy $E1$ transition. These transitions were not observed, because these transition are hindered for structural reasons. For example the $E1$ transition $^{7}/_{2}^{+} \rightarrow {}^{9}/_{2}^{-}$ requires significant structural changes $\pi(d_{3/2})^{-1} \otimes 2^{+} \rightarrow \pi(h_{9/2})$, but there is an alternative collective decay path to the $\pi(d_{3/2})^{-1}$ configuration that dominates.

5.3 Shears band in ^{201}At

Transitions (see Table 4.4) proposed to form a shears band show several properties, which are characteristic for bands originating from the shears mechanism. These properties were listed in section 2.5. Figure 5.4 shows the energies of the levels in the suggested shears band as a function of the level spin. The spin and energy assignments for the band-head state are tentative, but any change in them will shift the curve uniformly along the horizontal or vertical axis, respectively. The dashed lines in the figure represent two arbitrary parabolas. This parabolic behavior for $E(I)$ is one of the characteristic properties of the shears mechanism (See listed property number 1 in section 2.5). The bump close to spin $\sim 16\hbar$ is the result of a band crossing. This band crossing can also be seen in the inset of the Fig. 5.4 as a ”backbending”. The lengths of the shears ”blades” vary before and after the band crossing, hence reorienting the ”blades” by increasing the shears angle produces a state with the same angular momentum but lower energy.

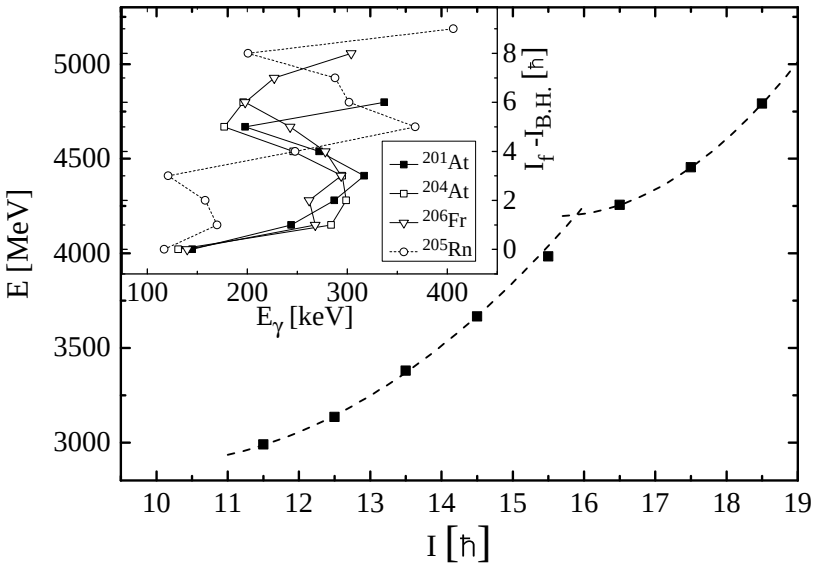

Figure 5.4: Level energies for the suggested shears band in ^{201}At as a function of the level spin. The spin and energy of the band-head state are tentative, but any change in spin (energy) will shift the curve along the horizontal (vertical) axis. The dashed line represents two arbitrary parabolas to guide the eye. The inset shows for each transition the final state spin I_f with respect to the band-head spin $I_{B.H.}$ as a function of the γ-ray energy. Data for ^{205}Rn are taken from [Novak99] and for ^{204}At and ^{206}Fr from [Hartley08]. The figure is from [Auranen15].

Based on the angular distribution of the γ-ray transitions and high x-ray yield, the transitions in the proposed shears band were identified as forming a rotational-like cascade of $M1$ transitions. The absence of the $E2$ crossover transitions suggests a high $B(M1)/B(E2)$ ratios, which can also be seen from the estimated lower limits presented in Table 4.4. High $B(M1)/B(E2)$ ratios are again one of the characteristic features for shears bands, see property number 2. However, with the current experimental setup it was not possible to measure the absolute values of $B(M1)$ or $B(E2)$.

The few lowest active shell model orbitals for protons in ^{201}At are $h_{9/2}$, $f_{7/2}$ and $i_{13/2}$. Among active neutron orbitals there are hole excitations from the $i_{13/2}$ orbital. These neutron excitations may require a breaking of a neutron pair, but excitation energies of $\sim 3-5$ MeV are enough to make this energetically

Table 5.3: Calculated band head state spin $I_{B.H.}$ and the maximum spin I_{MAX}, for selected proton and neutron configurations for the shears band in ^{201}At. Last column shows the sum of the proton and neutron state level energies. Proton state energies are taken from this work, and neutron state energies are taken from [Weckström85, Maj90]. Experimental band head state spin is $^{23}/_{2}$ $\hbar$ and it lies at the energy of 2990 keV. The observed band crossing takes place at the energy of $\sim$ 4200 keV and spin $\sim$16 $\hbar$.

$\|\pi\rangle$	$\|\nu\rangle$	$I_{\text{B.H.}}$ [$\hbar$]	I_{MAX} [$\hbar$]	$E_\pi + E_\nu$ [keV]
$\|i_{13/2}; 13/2^+\rangle$	$\|f_{5/2}^{-1} i_{13/2}^{-1}; 7^-\rangle$	9.7	14.0	2885
$\|i_{13/2}; 13/2^+\rangle$	$\|f_{5/2}^{-1} i_{13/2}^{-1}; 8^-\rangle$	10.5	15.0	2986
$\|i_{13/2}; 13/2^+\rangle$	$\|f_{5/2}^{-1} i_{13/2}^{-1}; 9^-\rangle$	11.3	16.0	3010
$\|(h_{9/2})^2 i_{13/2}; 29/2^+\rangle$	$\|f_{5/2}^{-1} i_{13/2}^{-1}; 5^-\rangle$	15.5	20.0	4130
$\|(h_{9/2})^2 i_{13/2}; 29/2^+\rangle$	$\|f_{5/2}^{-1} i_{13/2}^{-1}; 7^-\rangle$	16.3	22.0	4455
$\|(h_{9/2})^2 i_{13/2}; 29/2^+\rangle$	$\|f_{5/2}^{-1} i_{13/2}^{-1}; 8^-\rangle$	16.7	23.0	4556
$\|(h_{9/2})^2 i_{13/2}; 29/2^+\rangle$	$\|f_{5/2}^{-1} i_{13/2}^{-1}; 9^-\rangle$	17.2	24.0	4580

possible. The orbitals have high-j values, which are required to form a typical shears band (Property 4). The backbending in the inset of Fig. 5.4 is very similar in nuclei ^{204}At, ^{206}Fr and ^{201}At. This might indicate that the proton and neutron configurations associated with the shears mechanism in all of these nuclei are similar. In the earlier study of the shears mechanism in ^{204}At and ^{206}Fr [Hartley08] the single particle configurations remained unknown. In these nuclei most likely the $h_{9/2}$ and/or $i_{13/2}$ proton orbitals along with the $i_{13/2}$ neutron orbitals are involved in the configurations of the shears bands.

The shears angle for the band-head state in a shears band is $\sim$90°, hence equation 2.8 can be used to calculate band-head state spin for various single-particle configurations. Similarly, the maximum spin can be calculated by setting the shears angle to $\sim$0°. A selection of this kind of calculations is summarized in table 5.3, together with the sum of proton and neutron state level energies. The respective experimental values are $^{23}/_{2}$ $\hbar$ and 2990 keV for the band-head state, and $\sim$16 ħ and $\sim$4200 keV for the band crossing. Based on these calculations the suggested single particle configuration for the lower part of the cascade is $\pi(i_{13/2}) \otimes \nu(f_{5/2}^{-1} i_{13/2}^{-1})$, and $\pi((h_{9/2})^2 i_{13/2}) \otimes \nu(f_{5/2}^{-1} i_{13/2}^{-1})$ for

the higher part. These configurations yield a negative parity for the observed shears band. In various odd-mass lead isotopes lighter than $A = 197$ a similar alignment has been observed ([Görgen01], and references therein). In these nuclei the band crossing is caused by the alignment of neutrons in $i_{13/2}$ orbital.

Chapter 6

Summary and Outlook

In the present work ^{199}At and ^{201}At nuclei have been studied using fusion evaporation reactions and a gas-filled recoil separator. Three main results have been obtained: Firstly, an isomeric $^{29}/_{2}^{+}$ state in ^{201}At has been observed with a half life of 3.39(9) µs. The $^{29}/_{2}^{+}$ state is suggested as originating from the $\pi(h_{9/2}) \otimes |^{200}\text{Po}; 11^{-}\rangle$ configuration. The isomeric state is depopulated through 269-keV $E2$ and 339-keV $E3$ transitions with reduced transition strengths of $1.26(4) \cdot 10^{-3}$ W.u. and 21(3) W.u., respectively. Secondly, an isomeric intruder $^{1}/_{2}^{+}$ state has been observed in ^{201}At, and earlier knowledge of the same state in ^{199}At have been confirmed and improved. The isomer is suggested as originating from the $\pi(s_{1/2})^{-1}$ single particle configuration. The $^{1}/_{2}^{+}$ state decays through an $E3$ transition with a half-life and reduced transition strength of 273(9) ms, 45(3) ms and 0.09(2) W.u. 0.050(3) W.u. for ^{199}At and ^{201}At, respectively. In both nuclei the $^{1}/_{2}^{+}$ state is fed from nearly spherical $^{3}/_{2}^{+}$ and $^{5}/_{2}^{+}$ states most likely originating from the $\pi(d_{3/2})^{-1}$ and the $\pi(d_{5/2})^{-1}$ single particle configurations, respectively. Thirdly, perhaps the most remarkable result obtained in this study is that a cascade of magnetic dipole transitions has been observed, which is interpret as a shears band in ^{201}At. Generally speaking, the result achieved in this study agree well with the earlier results in the mentioned nuclei. Moreover, the results of this study are consistent when comparing to the neighboring nuclei, and the overall systematics of this part of nuclide chart.

In JYFL there is a long and successful history in the research of odd-mass nuclei above lead. Kettunen *et al.* have studied the decay properties of light astatine isotopes ^{191,193,195}At [Kettunen03a, Kettunen03b]. In a further study by Nyman *et al.* in-beam γ-ray spectroscopy has been performed for ^{195}At [Nyman13]. Two separate publications exist about the level structure of ^{197}At, one by Andgren *et al.* [Andgren08] and one by Jakobsson *et al.* [Jakobsson10]; the latter one also presents results for ^{199}At. In addition to these studies a number of experiments have been performed in the competing laboratories. Despite these high-quality spectroscopy studies the systematics of the low-lying states in odd-mass astatine nuclei is far from complete. The isomeric $^{29}/_{2}^{+}$ state is still unknown in ^{197,203,207}At nuclei. The information about the isomeric $^{25}/_{2}^{+}$ state is also incomplete in the astatine isotopes ^{197,203}At. The isomeric $^{1}/_{2}^{+}$ state is completely unknown in ^{203}At and heavier isotopes. Also the feeding of the $^{1}/_{2}^{+}$ state is unknown in ^{197}At. Further studies are needed in order to form a complete picture about the behavior of these levels and the overall structure of astatine nuclei. In order to fill a few gaps in knowledge of astatine nuclei we have planned an experiment that aims to study ^{197,203}At nuclei. The main goal of this experiment is to identify the so far unknown isomeric states, their decay and feeding. Also ^{203}At is a very good candidate nucleus for another shears band. Last autumn the proposal of this experiment was accepted by the JYFL PAC, and we look forward for the coming experiment, which will take place during early July 2015.

Bibliography

[Alvarez93] C. R. Alvarez. Nucl. Phys. News **3**, 10 (1993). doi:10.1080/10506899308221154.

[Andgren08] K. Andgren *et al.* Phys. Rev. C **78**, 044328 (2008). doi:10.1103/PhysRevC.78.044328.

[Andreyev04] A. Andreyev *et al.* Phys. Rev. C **69**, 054308 (2004). doi:10.1103/PhysRevC.69.054308.

[Auranen14] K. Auranen *et al.* Phys. Rev. C **90**, 024310 (2014). doi:10.1103/PhysRevC.90.024310.

[Auranen15] K. Auranen *et al.* Phys. Rev. C **91**, 024324 (2015). doi:10.1103/PhysRevC.91.024324.

[Batchelder99] J. Batchelder *et al.* Eur. Phys. J. A **5**, 49 (1999). doi:10.1007/s100500050255.

[Baxter90] A. Baxter *et al.* Nucl. Phys. A **515**, 493 (1990). doi:10.1016/0375-9474(90)90595-D.

[Beausang92] C. Beausang *et al.* Nucl. Instrum. Methods Phys. Res., Sect. A **313**, 37 (1992). doi:10.1016/0168-9002(92)90084-H.

[Bergström70] I. Bergström *et al.* Phys. Scr. **1**, 243 (1970). doi:10.1088/0031-8949/1/5-6/008.

[Bergström85] I. Bergström *et al.* Phys. Scr. **31**, 26 (1985). doi:10.1088/0031-8949/31/1/005.

[Bernstein95] L. A. Bernstein *et al.* Phys. Rev. C **52**, 621 (1995). doi:10.1103/PhysRevC.52.621.

[Beuscher76] H. Beuscher *et al.* Phys. Rev. Lett. **36**, 1128 (1976). doi:10.1103/PhysRevLett.36.1128.

[Bohr98] A. Bohr *et al.* Nuclear Structure, Volume II: Nuclear Deformations. World Scientific Publishing Co. Pte. Ltd., P.O. BOX 128, Farrer Road, Singapore 912805 (1998).

[Brandolini96] F. Brandolini *et al.* Phys. Lett. B **388**, 468 (1996). doi:10.1016/S0370-2693(96)01202-6.

[Centnerszwer15] M. Centnerszwer. Radiumi ja radioaktiiviset ilmiöt. Kustannusosakeyhtiö Otava, Helsinki, Finland (1915).

[Clark99] R. Clark *et al.* Phys. Rev. Lett. **82**, 3220 (1999). doi:10.1103/PhysRevLett.82.3220.

[Clark00] R. M. Clark *et al.* Annu. Rev. Nucl. Part. Sci. **50**, 1 (2000). doi:10.1146/annurev.nucl.50.1.1.

[Coenen85] E. Coenen *et al.* Phys. Rev. Lett. **54**, 1783 (1985). doi:10.1103/PhysRevLett.54.1783.

[Coenen86] E. Coenen *et al.* Z. Phys. A **324**, 485 (1986). doi:10.1007/BF01290933.

[Davie84] R. Davie *et al.* Nucl. Phys. A **430**, 454 (1984). doi:10.1016/0375-9474(84)90049-6.

[Dobson02] D. J. Dobson *et al.* Phys. Rev. C **66**, 064321 (2002). doi:10.1103/PhysRevC.66.064321.

[Duchêne99] G. Duchêne *et al.* Nucl. Instrum. Methods Phys. Res., Sect. A **432**, 90 (1999). doi:10.1016/S0168-9002(99)00277-6.

[Dybdal83] K. Dybdal *et al.* Phys. Rev. C **28**, 1171 (1983). doi:10.1103/PhysRevC.28.1171.

[Frauendorf93] S. Frauendorf. Nucl. Phys. A **557**, 259 (1993). doi:10.1016/0375-9474(93)90546-A.

[Gadea97] A. Gadea *et al.* Phys. Rev. C **55**, R1 (1997). doi:10.1103/PhysRevC.55.R1.

[Görgen01] A. Görgen *et al.* Nucl. Phys. A **683**, 108 (2001). doi:10.1016/S0375-9474(00)00470-X.

[Hartley08] D. J. Hartley *et al.* Phys. Rev. C **78**, 054319 (2008). doi:10.1103/PhysRevC.78.054319.

[Helariutta99] K. Helariutta *et al.* Eur. Phys. J. A **6**, 289 (1999). doi:10.1007/s100500050347.

[Heyde83] K. Heyde *et al.* Phys. Rep. **102**, 291 (1983). doi:10.1016/0370-1573(83)90085-6.

[Honkanen86] K. Honkanen *et al.* Nucl. Phys. A **451**, 141 (1986). doi:10.1016/0375-9474(86)90248-4.

[Jakobsson10] U. Jakobsson *et al.* Phys. Rev. C **82**, 044302 (2010). doi:10.1103/PhysRevC.82.044302.

[Jakobsson12] U. Jakobsson *et al.* Phys. Rev. C **85**, 014309 (2012). doi:10.1103/PhysRevC.85.014309.

[Jakobsson13] U. Jakobsson *et al.* Phys. Rev. C **87**, 054320 (2013). doi:10.1103/PhysRevC.87.054320.

[Jenkins98] D. Jenkins *et al.* Phys. Lett. B **428**, 23 (1998). doi:10.1016/S0370-2693(98)00384-0.

[Julin01] R. Julin *et al.* J. Phys. G **27**, R109 (2001). doi:10.1088/0954-3899/27/7/201.

[Kalaninová13] Z. Kalaninová *et al.* Phys. Rev. C **87**, 044335 (2013). doi:10.1103/PhysRevC.87.044335.

[Kettunen03a] H. Kettunen *et al.* Eur. Phys. A **17**, 537 (2003). doi:10.1140/epja/i2002-10162-1.

[Kettunen03b] H. Kettunen *et al.* Eur. Phys. J. A **16**, 457 (2003). doi:10.1140/epja/i2002-10130-9.

[Kibédi08] T. Kibédi *et al.* Nucl. Instrum. Methods Phys. Res., Sect. A **589**, 202 (2008). doi:10.1016/j.nima.2008.02.051.

[Kondev07] F. Kondev. Nucl. Data Sheets **108**, 365 (2007). doi:10.1016/j.nds.2007.01.004.

[Kondev11] F. Kondev *et al.* Nucl. Data Sheets **112**, 707 (2011). doi:10.1016/j.nds.2011.02.002.

[Kratschmer73] W. Kratschmer *et al.* Nucl. Phys. A **201**, 179 (1973). doi:10.1016/0375-9474(73)90695-7.

[Lane95] G. Lane *et al.* Nucl. Phys. A **586**, 316 (1995). doi:10.1016/0375-9474(94)00515-O.

[Lazarus01] I. Lazarus *et al.* IEEE Trans. Nucl. Sci. **48**, 567 (2001). doi:10.1109/23.940120.

[Leino95] M. Leino *et al.* Nucl. Instr. Methods Phys. Res., Sect. B **99**, 653 (1995). doi:10.1016/0168-583X(94)00573-7.

[Lilley02] J. Lilley. Nuclear Physics - Principles and Applications. John Wiley & Sons Ltd., West Sussex, England (2002).

[Magill12] J. Magill *et al.* Karlsruher Nuklidkarte. Nucleonica GmbH, Eggenstein-Leopoldshafen, Germany (2012).

[Maj90] A. Maj *et al.* Nucl. Phys. A **509**, 413 (1990). doi:10.1016/0375-9474(90)90430-T.

[Mann88] L. G. Mann *et al.* Phys. Rev. C **38**, 74 (1988). doi:10.1103/PhysRevC.38.74.

[Mateosian74] E. D. Mateosian *et al.* At. Data and Nucl. Data Tables **13**, 391 (1974). doi:10.1016/0092-640X(74)90007-2.

[Morinaga76] H. Morinaga *et al.* In-Beam Gamma-Ray Spectroscopy. North-Holland Publishing Company, Amsterdam, New York, Oxford (1976).

[nat08] Nature Physics **4**, 257 (2008). doi:10.1038/nphys921.

[Nieminen04] P. Nieminen *et al.* Phys. Rev. C **69**, 064326 (2004). doi:10.1103/PhysRevC.69.064326.

[Nilsson55] S. G. Nilsson. Det Konglige Danske Videnskabernes Selskab **29**, 1 (1955).

[Nilsson95] S. G. Nilsson *et al.* Shapes and Shells in Nuclear Structure. Cambridge University Press, The Edinburgh Building, Cambridge CB2 2RU, UK (1995).

[Novak99] J. R. Novak *et al.* Phys. Rev. C **59**, R2989 (1999). doi:10.1103/PhysRevC.59.R2989.

[Nudat2.6] Nudat2.6. `http://www.nndc.bnl.gov/nudat2/`.

[Nyman13] M. Nyman *et al.* Phys. Rev. C **88**, 054320 (2013). doi:10.1103/PhysRevC.88.054320.

[Page03] R. Page *et al.* Nucl. Instrum. Methods Phys. Res., Sect. B **204**, 634 (2003). doi:10.1016/S0168-583X(02)02143-2.

[Poletti97] A. Poletti *et al.* Nucl. Phys. A **615**, 95 (1997). doi:10.1016/S0375-9474(96)00428-9.

[Preston62] M. A. Preston. Physics of the Nucleus. Addison-Wesley Publishing Company, Inc., Reading, Massachusetts (1962).

[Rahkila08] P. Rahkila. Nucl. Instrum. Methods Phys. Res., Sect. A **595**, 637 (2008). doi:10.1016/j.nima.2008.08.039.

[Rainwater50] J. Rainwater. Phys. Rev. **79**, 432 (1950). doi:10.1103/PhysRev.79.432.

[Ruotsalainen13] P. Ruotsalainen. Doctoral thesis. University of Jyväskylä, Jyväskylä, Finland (2013).

[Rutherford11] E. Rutherford. Phil. Mag. **21**, 669 (1911).

[Sarén11] J. Sarén *et al.* Nucl. Instr. Methods Phys. Res., Sect. A **654**, 508 (2011). doi:10.1016/j.nima.2011.06.068.

[Schmidt00] K. Schmidt. The European Physical Journal A **8**, 141 (2000). doi:10.1007/s100500070129.

[Singh07] B. Singh. Nuclear Data Sheets **108**, 79 (2007). doi:10.1016/j.nds.2007.01.001.

[Sjoreen76] T. Sjoreen *et al.* Phys. Rev. C **14**, 1023 (1976). doi:10.1103/PhysRevC.14.1023.

[Sjoreen81] T. P. Sjoreen *et al.* Phys. Rev. C **23**, 272 (1981). doi:10.1103/PhysRevC.23.272.

[Sjoreen82] T. P. Sjoreen *et al.* Phys. Rev. C **25**, 889 (1982). doi:10.1103/PhysRevC.25.889.

[Suhonen07] J. Suhonen. From nucleons to nucleus. Springer-Verlag, Berlin, Germany (2007).

[Uusitalo05] J. Uusitalo *et al.* Phys. Rev. C **71**, 024306 (2005). doi:10.1103/PhysRevC.71.024306.

[Uusitalo13] J. Uusitalo *et al.* Phys. Rev. C **87**, 064304 (2013). doi:10.1103/PhysRevC.87.064304.

[Van de Vel03] K. Van de Vel *et al.* Eur. Phys. J. A **17**, 167 (2003). doi:10.1140/epja/i2003-10002-x.

[Weckström85] T. Weckström *et al.* Z. Phys. A **321**, 231 (1985). doi:10.1007/BF01493443.

[Wood92] J. Wood *et al.* Phys. Rep. **215**, 101 (1992). doi:10.1016/0370-1573(92)90095-H.